JOURNAL OF COMPUTATIONAL PHYSICS **128,** 101–120 (1996)
ARTICLE NO. 0198

A Synchronous and Iterative Flux-Correction Formalism for Coupled Transport Equations

CHRISTOPH SCHÄR* AND PIOTR K. SMOLARKIEWICZ†,[2]

*Atmospheric Physics ETH, 8093 Zürich, Switzerland; †National Center for Atmospheric Research,[1] Boulder, Colorado
E-mail: schaer@atmos.umnw.ethz.ch

Received January 23, 1995; revised March 21, 1996

Many problems of fluid dynamics involve the coupled transport of several, density-like, dependent variables (for instance, densities of mass and momenta in elastic flows). In this paper, a conservative and synchronous flux-corrected transport (FCT) formalism is developed which aims at a consistent transport of such variables. The technique differs from traditional FCT algorithms in two respects. First, the limiting of transportive fluxes of the primary variables (e.g., mass and momentum) does not derive from smooth estimates of the variables, but it derives from analytic constraints implied by the Lagrangian form of the governing continuity equations, which are imposed on the specific mixing ratios of the variables (e.g., velocity components). Second, the traditional FCT limiting based on sufficiency conditions is augmented by an iterative procedure which approaches the necessity requirements. This procedure can also be used in the framework of traditional FCT schemes, and a demonstration is provided that it can significantly reduce some of the pathological behaviors of FCT algorithms. Although the approach derived is applicable to the transport of arbitrary conserved quantities, it is particularly useful for the synchronous transport of mass and momenta in elastic flows, where it assures intrinsic stability of the algorithm regardless of the magnitude of the mass-density variable. This latter property becomes especially important in fluids with large density variations, or in models with a material "vertical" coordinate (e.g., geophysical hydrostatic stratified flows in isopycnic/isentropic coordinates), where material surfaces can collapse to zero-mass layers admitting, therefore, arbitrarily large local Courant numbers.

1. INTRODUCTION

The usefulness of numerical transport algorithms has traditionally been judged from the key properties of numerical analysis which relate to stability, consistency, characteristics of conservation, and order of accuracy. It has, however, been recognized for some time that the performance of schemes often depends on "behavioral errors" [24] as well. Of particular importance is the representation of properties which either derive analytically from the governing set of equations, or which have some useful numerical characteristics otherwise. Examples include the positive definiteness of a scheme, or monotonicity and total variation diminishing constraints. These constraints are violated by linear higher-order numerical approximations [11].

Powerful methods nowadays allow for the implementation of various constraints into numerical schemes. One method of wide applicability and of particular importance to the present study is the flux-corrected transport (FCT) originated by Boris and Book [5–7] and generalized by Zalesak [36]. Succinct reviews of this technique can be found in [31, 19, 35]. In geophysical applications, consideration is typically given to the transport problem

$$\frac{\partial \rho}{\partial t} + \nabla \cdot (\mathbf{v}\rho) = 0, \tag{1.1}$$

where $\mathbf{v}$ is an externally specified velocity vector and ρ is an arbitrary density-like dependent variable. The FCT technique makes comparative use of both a first-order and a higher-order time-step, and it ensures in effect that new local extremes in the higher order integration of ρ can only develop if they do so already in the first-order time-step. This is a heuristic approach, but it is very successful in providing smooth and nonlinearly stable integrations (cf. [30] for a discussion).

The original studies on FCT had a scope of a single transport equation, but more recently some coupled systems have also been treated. Here consideration will be given to the reduced set of elastic flow equations

$$\frac{\partial \rho}{\partial t} + \nabla \cdot (\mathbf{v}\rho) = 0, \tag{1.2}$$

$$\frac{\partial V_l}{\partial t} + \nabla \cdot (\mathbf{v}V_l) = R_l \quad \text{for } l = 1, L, \tag{1.3}$$

where ρ denotes a density-like variable, and $V_l = \rho v_l$ denotes the momentum components. In general, the forcing term R_l in (1.3) combines the pressure, buoyancy, and nonconservative forces. A related system, namely the compressible Euler equations, has been analysed by Löhner *et*

[1] The National Center for Atmospheric Research is sponsored by the National Science Foundation.

0021-9991/96 $18.00

al. [19]. They noted that the independent application of the FCT procedure to the individual equations produces an excessive amount of "ripples" in the non-conserved quantities (such as $\mathbf{v}$), and ultimately in the conserved quantities as well. Furthermore, they have concluded that the use of the same coefficients for the FCT limiting of the advective fluxes of all transported variables does greatly improve the results. Related synchronization concepts have also been employed by Harten and Zwaas [14] in the context of their hybrid scheme. Another successful approach is that followed by Grabowski and Smolarkiewicz [12], who applied FCT techniques to treat the combined advection–condensation problem as it is posed by the water substance in atmospheric numerical models. However, as their FCT procedure makes explicit use of the specific forcings for the problem at hand, they cannot be directly extended to a general problem of the form (1.2)–(1.3).

The difficulties which arise from full systems of equations are due to the dynamical coupling. In the case of (1.2)–(1.3), the coupling occurs for two reasons, namely (i) through the forcing terms $\mathbf{R}$ and (ii) through the velocity $\mathbf{v} = \mathbf{V}/\rho$ itself. Unlike some studies of compressible gas dynamics (cf. [15, 22]), the current paper considers exclusively the coupling of category (ii), and the forcings in (1.3) will hence be dropped.

With $\mathbf{R} = 0$, the system (1.2)–(1.3) is formally identical to the simultaneous transport of the density ρ and some additional conserved quantities (hereafter, substances A_l for brevity), i.e.,

$$\frac{\partial \rho}{\partial t} + \nabla \cdot (\mathbf{v}\rho) = 0, \tag{1.4}$$

$$\frac{\partial A_l}{\partial t} + \nabla \cdot (\mathbf{v}A_l) = 0 \quad \text{for } l = 1, L, \tag{1.5}$$

where the velocity-field is assumed to be prescribed. Unlike the treatment in [19], the technique to be developed in the current paper is not based on the traditional FCT limiting conditions for A_1 and ρ, but rather on a consistency relation between A_l and ρ. This relation follows by converting (1.5) into the Lagrangian form

$$\frac{d}{dt}\left(\frac{A_l}{\rho}\right) = 0 \tag{1.6}$$

which expresses the conservation of the substances' mixing ratios A_l/ρ along flow trajectories. It implies that the value of A_l/ρ at time $t + \Delta t$ is bound by the values in the immediate environment at time t. Further, in this paper, for the sake of brevity, such a property will be referred to as *compatibility*. Although FCT transport algorithms are often referred to as monotonicity-preserving schemes, the latter term merely refers to a smoothness of numerical solutions. In contrast, our compatibility retains more of the precise meaning of monotonicity as it ensures a property which directly derives from the governing system of equations and does not rely on a first-order time-step.

In either incompressible or anelastic fluid problems, the compatibility constraint can be easily incorporated in the traditional FCT algorithms of Zalesak [36] (cf. Section 3.1 in [31] for a discussion). In arbitrary fluid problems, it can be met fairly easily in semi-Lagrangian models which integrate the material form of the governing fluid equations [32, 34]. In contrast, in the context of elastic fluids in conservative Eulerian formulation, implementation of the compatibility constraint is not necessarily a trivial task, as it depends on several prognostic variables. One approach to the problem was recently outlined by Larrouturou [18], who considered the problem of a gaseous mixture of several species. He ensured that all the fluxes in the continuity and constituents equations correspond to the same discrete mass flux, and thereby obtained a scheme that guarantees monotone and positive definite transport of the individual mass fractions.

In contrast to [18], our implementation of the compatibility constraint follows classical FCT ideas, at least to the extent that flux-limiting coefficients are separately computed for the incoming and outgoing fluxes. This approach, which is the foundation of all FCT algorithms, is based on sufficiency rather than necessity conditions. This implies that some portion of the fluxes may unjustifiably be rejected and indicates that FCT algorithms are in general more diffusive than they would need to be in order to achieve the desired property. More seriously, this diffusive effect can be highly localized, and this can lead to pathological behaviors. For instance, it is well known that the advection of a simple sinusoidal anomaly with FCT does introduce serious distortions, such that the advected sine curve finally resembles a sawtooth-like pattern. Here it will be demonstrated how the classical FCT treatment can be augmented by an iterative procedure which approaches the necessity requirements and reduces the diffusive effects. This treatment is of interest beyond the compatibility constraint addressed in this paper and is applicable in the framework of other FCT algorithms.

Several sophisticated high-resolution finite difference transport schemes (see [20] for a succinct review) have been suggested in recent years. The purpose of the current paper is not to provide yet another such scheme, nor to address the competitiveness of a particular scheme, but rather to extend the existing basic FCT methodology to a broad and important class of applications. The ideas proposed are applicable in essence with any FCT algorithm. For the examples provided in the paper we have selected two schemes to provide the underlying higher-order fluxes, namely one scheme which is by itself almost

compatible (the second-order positive definite MPDATA scheme [28]) and one scheme which is by itself far from being compatible (the Lax–Wendroff scheme [24] enhanced with classical FCT).

The outline of the paper is as follows: In Section 2, a more thorough definition of compatibility follows, together with numerical examples which demonstrate that compatibility can indeed be a crucial issue. The synchronous flux correction technique will be derived in Section 3. In Section 4 consideration will be given to the iterative application of flux corrections. Some numerical tests then follow in Section 5, and the study is concluded in Section 6. Some mathematical details are referred to the appendices.

2. COMPATIBILITY

2.1. *Definition*

Consider a finite-difference numerical integration of the system (1.4)–(1.5) in two-dimensional geometry and with dimensionless grid-spacings and time-step $(\Delta x, \Delta y, \Delta t) = (1, 1, 1)$. The discretization takes the form

$$\psi_{i,j}^n = \psi|_{x=i,\, y=j,\, t=n}, \tag{2.1}$$

where the symbol ψ stands for any of the variables ρ and A_l.

Under "compatible transport" we understand a numerical integration of (1.4)–(1.5) which is consistent with the advective form (1.6) of Eq. (1.4). More precisely, in a finite difference approximation which is subject to the CFL criterion, information can travel at most over one grid-box per time-step. It then follows from (1.6) that the value of the mixing ratio

$$a_l := A_l/\rho \tag{2.2}$$

at time-level $n + 1$ is limited by the values of a_l at time-level n at the surrounding grid-points. This is expressed as

$$(a_l)_{i,j}^{\min,n+1} \le (a_l)_{i,j}^{n+1} \le (a_l)_{i,j}^{\max,n+1}, \tag{2.3}$$

with

$$(a_l)_{i,j}^{\min,n+1} := \min_{\substack{|i-i'|\le 1\\ |j-j'|\le 1}} \{(a_l)_{i',j'}^n\}, \tag{2.4a}$$

$$(a_l)_{i,j}^{\max,n+1} := \max_{\substack{|i-i'|\le 1\\ |j-j'|\le 1}} \{(a_l)_{i',j'}^n\}, \tag{2.4b}$$

where (i', j') excludes grid-points with $\rho = 0$, where the mixing ratios are ill-defined.

Unlike in traditional flux-corrected transport [12], the bounds appearing in (2.4) are available prior to execution of *any* time-step and do not depend on first-order estimates, as in traditional flux-corrected transport [12]. Instead they derive from the Lagrangian form of the transport equations.

2.2. *Example*

Although compatibility is an obvious property of the coupled system (1.4)–(1.5), it is violated by most conservative numerical techniques. In fact, the only compatible and conservative finite-difference scheme which we are aware of is the first-order upstream scheme. For this scheme, compatibility can formally be established (for an outline of the proof see Appendix A). For a brief demonstration of some of the difficulties which occur with incompatible schemes we now turn our attention to an idealized deformation test. Consideration is given to a system of two one-dimensional transport equations

$$\frac{\partial \rho}{\partial t} + \frac{\partial (u\rho)}{\partial x} = 0, \quad \frac{\partial A}{\partial t} + \frac{\partial (uA)}{\partial x} = 0, \tag{2.5}$$

with an externally specified deformation-flow of the form

$$u(x) = -x.$$

For arbitrary initial conditions $\rho_o(x)$ and $A_0(x)$ valid at time $t = 0$, the closed-form solution is

$$\rho(x, t) = e^t \rho_o(xe^t), \quad A(x, t) = e^t A_o(xe^t). \tag{2.6}$$

These formulae express that the shape of the anomaly remains unchanged except for some shrinking in the x-direction and an associated change in amplitude. Throughout the evolution, the mixing ratio $a = A/\rho$ obeys

$$a(x, t) = a_o(xe^t) \tag{2.7}$$

and remains globally bounded by its initial extrema. Here we again use the convention that lower-case a_l denote the mixing ratios and upper-case A_l denote the concentrations.

The initial conditions to be used in the following finite difference tests are sketched in Fig. 1. The initial distribution of the density-field ρ is specified as a localized anomaly surrounded by "vacuum"; i.e.,

$$\rho_o(x) = \begin{cases} 1 - x & \text{for } -1 \le x \le 0 \\ 1 & \text{for } 0 \le x \le 1, \\ 0 & \text{otherwise,} \end{cases} \tag{2.8}$$

while the mixing ratio is specified as a symmetrical step-type function

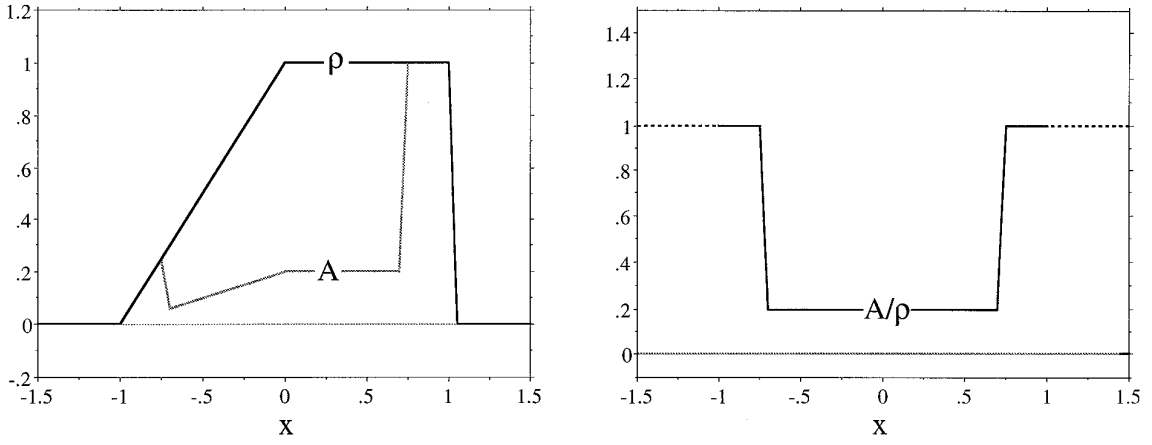

FIG. 1. Initial conditions for the deformation test. The left-hand panel shows the density ρ and the concentration A, the right-hand panel shows the mixing-ratio $a = A/\rho$.

$$a_o(x) = \begin{cases} 1 & \text{for } |x| \geq 0.75 \\ 0.2 & \text{otherwise.} \end{cases} \tag{2.9}$$

Physically speaking, the mixing ratio a_o is ill-defined in the massless regions at $|x| > 1$ (indicated in Fig. 1 by the dotted line). This situation has already been alluded to at the end of Section 2.1, and some implications will later be discussed in Section 5.1.

For the numerical tests, a grid spacing of $\Delta x = 0.05$ and a time step of $\Delta t = 0.025$ are adopted, and the integrations are carried out over 40 time steps to $t = 1$. The computational domain is given by $|x| \leq 1.5$, but only the central portion of it is shown in the diagrams. The first two tests, shown in Fig. 2a and Fig. 2b, are based on the numerical integration of (2.5) with the first-order upstream scheme and the second-order positive definite MPDATA scheme [28] with two corrective iterations (IORD = 2), respectively. The panels on the left-hand side depict the density ρ and the concentration A. The mixing ratio of A is shown in the right-hand panels. For the sake of coding efficiency it is here defined as

$$a = \frac{A}{\rho + \varepsilon} \quad \text{with } \varepsilon = 10^{-15}. \tag{2.10}$$

The diagrams are displayed in a stretched fashion (note labels on the axes) such that the shape of the analytical solution does match that of the initial conditions in Fig. 1. As a result of this stretching, the number of grid-points visible in the diagram is reduced from 61 in Fig. 1 to 23 in Fig. 2.

For the upstream experiment in Fig. 2a, the distribution of A and ρ reveals significant implicit diffusion. Nevertheless, the mixing ratio remains globally bounded accordingly to (2.7) and (2.9) by

$$0.2 \leq a(x, t) \leq 1. \tag{2.11}$$

The conservation of these bounds is a result of the upstream scheme being compatible. On the other hand, the second-order MPDATA scheme, while reducing the amount of implicit diffusion, results in significant violations of (2.11). The maximum violation is $a = 1.248$ and it occurs near the left-hand flank of the anomaly, at a grid-point with $\rho = 0.056$ (cf. Fig. 2b, right-hand panel). This violation arises from incompatibilities between the transport of A and ρ.

Compatibility is not restored by classical flux-correction. For demonstration, Fig. 3 shows the results of the deformation test for FCT-versions of MPDATA (left-hand panels) and of the one-step Lax–Wendroff scheme [24] (right-hand panels). Since the distributions of ρ and A are similar to that shown in Fig. 2b (left-hand panel), only the mixing ratio is shown. The panels in (a) are for classical flux correction according to [31, 6, 36]. For the MPDATA-scheme, it is evident that the application of classical flux-correction in fact amplifies the incompatibilities between the two transported quantities. The maximum violation of (2.11) is now $a = 1.391$ as compared to $a = 1.248$ without flux correction. For the regular (no FCT) Lax–Wendroff scheme the results are disastrous since the scheme is not sign-preserving. When sign-preservation is restored by FCT (right-hand panels in Fig. 3) the violation of compatibility is also pronounced, and values of $a > 100$ are obtained.

The panels in Fig. 3b are for synchronized flux-correction according to Löhner *et al.* [19]. Their procedure involves the use of the same flux-correction coefficients

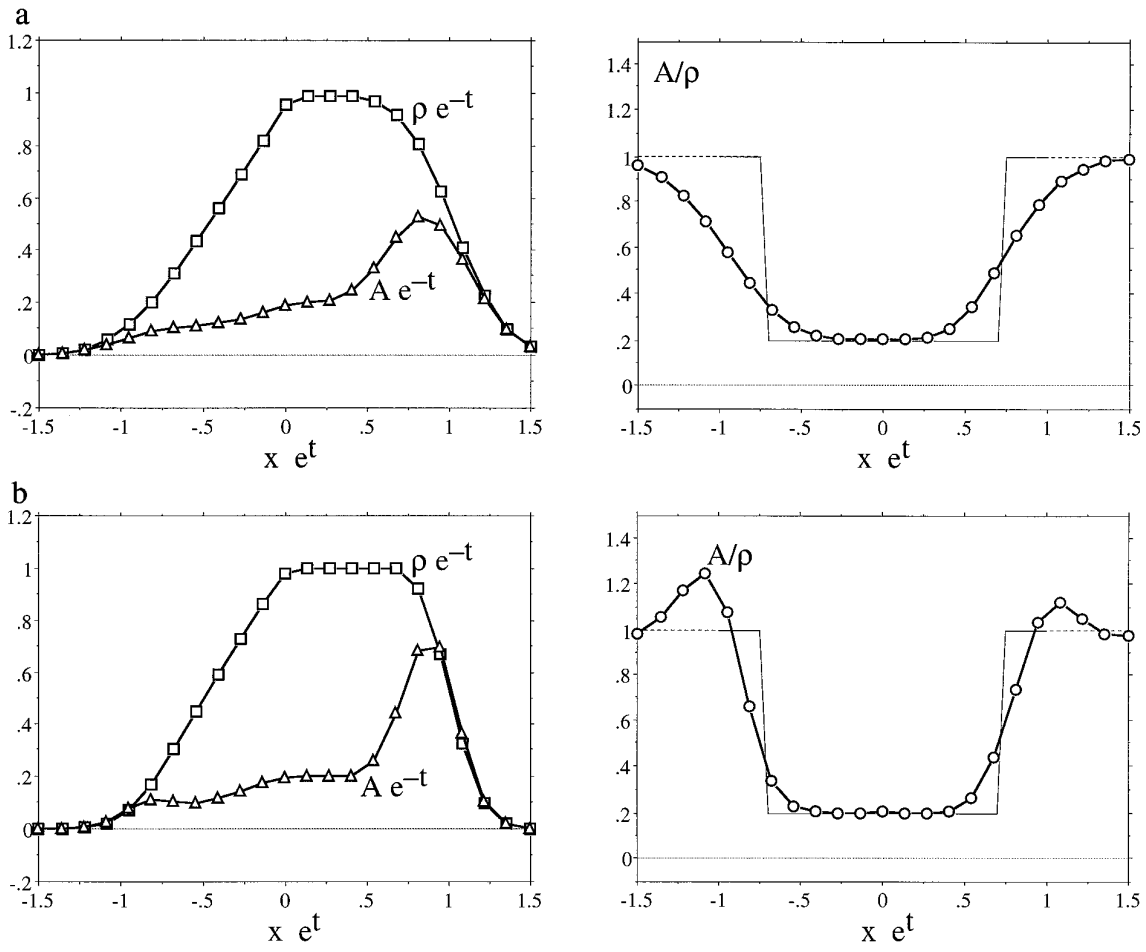

FIG. 2. Numerical solution to the deformation test at time $t = 1$. In (a), the fields A and ρ are transported by using the first-order upstream scheme. In (b), the second-order MPDATA scheme [28] is used instead. The left- and right-hand panels are in the same format as in Fig. 1, except for some shrinking in the x-axes (note labels). The thin line in the right-hand panels is the analytical solution.

$$\beta_i^{\mathrm{OUT}} = \min\{\beta_i^{\rho,\mathrm{OUT}}, \beta_i^{A,\mathrm{OUT}}\},$$
$$\beta_i^{\mathrm{IN}} = \min\{\beta_i^{\rho,\mathrm{IN}}, \beta_i^{A,\mathrm{IN}}\}, \tag{2.12}$$

for both the equations. Here $\beta^{\rho,\mathrm{OUT}}$ and $\beta^{\rho,\mathrm{IN}}$ denote the classical correction coefficients for, respectively, the outgoing and incoming fluxes of the ρ-equation (see (3.7) in Section 3). It can be seen from Fig. 3b, that this synchronization is indeed highly beneficial. In the case of the MPDATA scheme, the maximum violation of (2.11) is reduced to $a = 1.081$. In the case of the Lax–Wendroff scheme, the improvement is also remarkable. Although the maximum violation of a is still large, it occurs further away from the anomaly in a low-density environment.

It is quite typical that the violation of compatibility is strongest in the almost massless regions near the edge of the anomaly, where the density variable rapidly changes by many orders of magnitude. It depends on the nature of the application whether such incompatibilities are tolerable or not. Consider, for instance, the instantaneous release of a gas into the vacuum. Here the variables to be transported are mass and momentum, and the properties of the gas-front will heavily depend on the conservation of both these quantities. Incompatibilities can have serious consequences on the stability of the algorithm, since the "mixing ratio" of momentum corresponds to the velocity and defines the stability of the scheme through the Courant–Friedrichs–Levy criterion.

The discussion of the deformation test will be resumed in Section 5.1, where the compatible synchronization technique to be developed below will be evaluated.

3. A SYNCHRONOUS AND COMPATIBLE FLUX-CORRECTION FORMALISM

Consider the numerical integration of (1.4)–(1.5) that involves a first-order time-step followed by a second-order corrective-step. For the variables $\psi = \{\rho, A_l\}$ this is

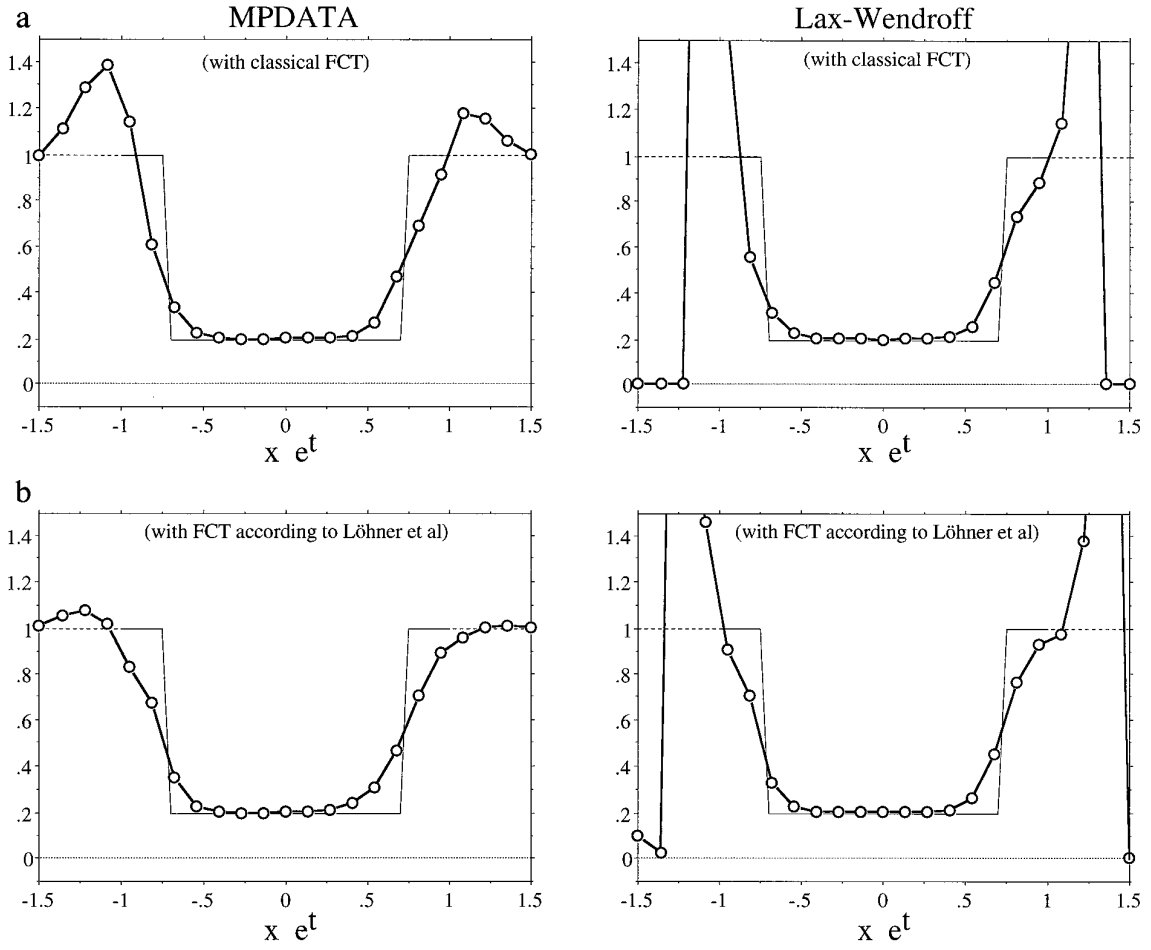

FIG. 3. The mixing-ratio $a = A/\rho$ for the deformation test with the MPDATA scheme (left-hand panels) and the Lax–Wendroff scheme (right-hand panels). In (a), the fluxes of these schemes are subject to classical flux correction [6, 7, 36]. In (b), the synchronization suggested by [19] is employed.

$$\psi_{i,j}^{n+1} = \psi_{i,j}^{0^{n+1}} + \psi_{i,j}'^{n+1}, \tag{3.1}$$

where ψ^0 and ψ denote the first- and higher order approximations, respectively. The higher order correction ψ' is given as the convergence of the anti-diffusive fluxes on a two-dimensional staggered mesh, i.e.,

$$\psi_{i,j}' = F_{i-1/2,j}^{\psi,1} - F_{i+1/2,j}^{\psi,1} + F_{i,j-1/2}^{\psi,2} - F_{i,j+1/2}^{\psi,2}, \tag{3.2}$$

where the two superscripts of the flux $\mathbf{F}$ refer to the quantity under consideration (i.e., ρ or one of the A_l-substances) and to the component of the flux, respectively. Note that for ease of notation we will suppress the time-level superscripts $n + 1$ wherever possible.

The form (3.1) is also formally applicable to schemes which do not explicitly involve the computation of the first-order approximation ψ^0. More generally, the only formal requirement to be utilized below is that $\psi^0 = \{\rho^0, A_l^0\}$ is compatible, i.e., satisfies relation (2.3) in the form

$$\left(\frac{A_l}{\rho}\right)_{i,j}^{\min,n+1} \le \left(\frac{A_l^0}{\rho^0}\right)_{i,j}^{n+1} \le \left(\frac{A_l}{\rho}\right)_{i,j}^{\max,n+1}. \tag{3.3}$$

Otherwise ψ^0 and ψ' can represent an arbitrary splitting of an arbitrary order of accuracy numerical scheme. This property of the present derivation will further be utilized in Section 4, but for the current subsection one can think of ψ^0 and ψ as first- and second-order approximations, respectively.

Incompatibilities, i.e. violations of (2.3), arise from the inadequate estimation of the higher-order anti-diffusive fluxes $\mathbf{F}^{\psi}$. The aim of the flux-correction technique is thus to reduce these fluxes by some factor β, e.g.,

$$\tilde{F}_{i+1/2,j}^{\psi,1} = \beta_{i+1/2,j}^{\psi,1} F_{i+1/2,j}^{\psi,1}, \tag{3.4}$$

such that (2.3) is met. As in classical flux-correction, it is stipulated that

$$0 \le \beta^{\psi,1}_{i+1/2,j} \le 1, \tag{3.5}$$

where $\beta \equiv 0$ and $\beta \equiv 1$ recover the first-order and the full second-order approximations, respectively. The flux-corrected time-step is then given by (cf. 3.1)

$$\hat{\psi}_{i,j} = \psi^0_{i,j} + \tilde{\psi}'_{i,j}, \tag{3.6}$$

where $\tilde{\psi}'$ denotes the convergence of the corrected fluxes $\tilde{\mathbf{F}}^{\psi}$, and $\hat{\psi}$ is the flux-corrected second-order approximation.

An important objective of flux-correction is the maximization of β (in some loose sense to be discussed later) in order to keep the numerical scheme as inviscid as possible. Following the pioneering work of Boris and Book [6, 7] and Zalesak [36] the flux-limiting operation (3.4) will be cast into the form

$$\begin{aligned}\tilde{F}^{\psi,1}_{i+1/2,j} = {} & (F^{\psi,1}_{i+1/2,j})^{+}\min\{1, \beta^{\psi,\mathrm{OUT}}_{i,j}, \beta^{\psi,\mathrm{IN}}_{i+1,j}\} \\ & + (F^{\psi,1}_{i+1/2,j})^{-}\min\{1, \beta^{\psi,\mathrm{IN}}_{i,j}, \beta^{\psi,\mathrm{OUT}}_{i+1,j}\},\end{aligned} \tag{3.7a}$$

$$\begin{aligned}\tilde{F}^{\psi,1}_{i,j+1/2} = {} & (F^{\psi,1}_{i,j+1/2})^{+}\min\{1, \beta^{\psi,\mathrm{OUT}}_{i,j}, \beta^{\psi,\mathrm{IN}}_{i,j+1}\} \\ & + (F^{\psi,1}_{i,j+1/2})^{-}\min\{1, \beta^{\psi,\mathrm{IN}}_{i,j}, \beta^{\psi,\mathrm{OUT}}_{i,j+1}\},\end{aligned} \tag{3.7b}$$

where

$$\chi^{+} = \max\{0, \chi\}, \quad \chi^{-} = \min\{0, \chi\} \tag{3.8}$$

denote the non-negative and non-positive part of χ. The approach exposed by (3.7) establishes, for each of the variables $\psi = \{\rho, A_l\}$, two correction coefficients, $\beta^{\psi,\mathrm{IN}}$ and $\beta^{\psi,\mathrm{OUT}}$, at every grid point, which are used for the limiting of incoming and outgoing fluxes, respectively. The term $\beta^{\psi,\mathrm{OUT}}$ represents the maximum fraction of the outgoing fluxes at a point that can be allowed without violating the constraint (2.3) at this particular point, while $\beta^{\psi,\mathrm{IN}}$ represents a similar quantity for the incoming fluxes. Taking the minimum in the way described by (3.7) ensures that all the constraints are satisfied. The appearance of unity in the min-function ensures that (3.5) is met.

In contrast to classical flux-correction, the correction factors β depend on several coupled equations. This is brought out after using (3.6) to cast the compatibility condition (2.3) into the form

$$(a_l)^{\min}_{i,j} \le \frac{(A^0_l)_{i,j} + (\tilde{A}'_l)_{i,j}}{\rho^0_{i,j} + \tilde{\rho}'_{i,j}} \le (a_l)^{\max}_{i,j}. \tag{3.9}$$

Some simple manipulations of (3.9) then yield the inequalities

$$(a_l)^{\min}_{i,j}\rho^0_{i,j} - (A^0_l)_{i,j} \le (\tilde{A}'_l)_{i,j} - (a_l)^{\min}_{i,j}\tilde{\rho}'_{i,j}, \tag{3.10a}$$

$$(a_l)^{\max}_{i,j}\rho^0_{i,j} - (A^0_l)_{i,j} \ge (\tilde{A}'_l)_{i,j} - (a_l)^{\max}_{i,j}\tilde{\rho}'_{i,j}. \tag{3.10b}$$

This form of (2.3) serves to separate the terms that can directly be computed from the first-order time step (on the left-hand side) from those which are affected by the flux-correction (on the right-hand side). It is apparent from this equation that the flux-correction associated with either one of the variables ρ or A_l can contribute to satisfy (3.10). Some concept is therefore required as to how to distribute the flux correction onto the variables. Here we have followed an idea that could be termed "equitable flux limiting." It is based on the recognition that it is not possible to figure out to what amount the two equations are responsible for a violation of (3.10), and it aims at establishing similar correction-coefficients β for the various variables.

For brevity the derivation of the correction coefficients is referred to Appendix B. In the case of $L = 1$ substance equation of type (1.5), the correction coefficients appearing in (3.7) for substance A are given by

$$\beta^{A,\mathrm{OUT}}_{i,j} = \frac{a^{\min}_{i,j}\rho^0_{i,j} - A^0_{i,j}}{A^{\mathrm{out}}_{i,j} - (a^{\min}_{i,j})^{+}\rho^{\mathrm{in}}_{i,j} - (a^{\min}_{i,j})^{-}\rho^{\mathrm{out}}_{i,j} - \varepsilon}, \tag{3.11a}$$

$$\beta^{A,\mathrm{IN}}_{i,j} = \frac{a^{\max}_{i,j}\rho^0_{i,j} - A^0_{i,j}}{A^{\mathrm{in}}_{i,j} - (a^{\max}_{i,j})^{+}\rho^{\mathrm{out}}_{i,j} - (a^{\max}_{i,j})^{-}\rho^{\mathrm{in}}_{i,j} + \varepsilon}. \tag{3.11b}$$

Here ε is a small number (e.g., $\varepsilon = 10^{-20}$), and the terms $\psi^{\mathrm{in}}_{i,j}$ and $\psi^{\mathrm{out}}_{i,j}$ denote the contributions of the in- and outgoing fluxes to $\psi'_{i,j}$ as defined by (B2). The correction coefficients for the density ρ can be computed from those of A with

$$\beta^{\rho,\mathrm{IN}}_{i,j} = \min\{\beta^{A,\mathrm{IN}}_{i,j} + \mathrm{sign}^{+}(a^{\max}_{i,j}), \beta^{A,\mathrm{OUT}}_{i,j} - \mathrm{sign}^{-}(a^{\min}_{i,j})\}, \tag{3.12a}$$

$$\beta^{\rho,\mathrm{OUT}}_{i,j} = \min\{\beta^{A,\mathrm{OUT}}_{i,j} + \mathrm{sign}^{+}(a^{\min}_{i,j}), \beta^{A,\mathrm{IN}}_{i,j} - \mathrm{sign}^{-}(a^{\max}_{i,j})\}. \tag{3.12b}$$

Here

$$\mathrm{sign}^{+}(\chi) = [\mathrm{sign}(\chi)]^{+} = \begin{cases} 1 & \text{if } \chi \ge 0 \\ 0 & \text{if } \chi < 0 \end{cases} \tag{3.13a}$$

$$\mathrm{sign}^{-}(\chi) = [\mathrm{sign}(\chi)]^{-} = \begin{cases} 0 & \text{if } \chi > 0 \\ -1 & \text{if } \chi \le 0 \end{cases} \tag{3.13b}$$

is a flag indicating the sign of a number. Equation (3.12) is in essence the coding-efficient form of a conditional Min-statement. The $\mathrm{sign}^{\pm}$-functions (including their leading signs) have always the values +1 or 0. In the first case, the

corresponding term does not contribute towards reducing β^ρ below 1 (i.e., the term is inactive), while in the second case the corresponding term is active and feeds a value of β^A into β^ρ. The simple form of (3.12) is of practical importance since the expensive computations in (3.11) only occur for the substance equation, but not for the continuity equation. In coding (3.12), care should be exercised with the sign$^\pm$-function. Note in particular that $\text{sign}^+(0) = -\text{sign}^-(0) = 1$.

Equation (3.12) implies that each of the two limiting coefficients for ρ is either larger than unity (and does not contribute to reducing the fluxes), or equal to one of the two limiting coefficients of A, e.g., $\beta_{i,j}^{\rho,\text{IN}} = \beta_{i,j}^{A,\text{OUT}}$ or $\beta_{i,j}^{\rho,\text{IN}} = \beta_{i,j}^{A,\text{IN}}$. This feature illustrates the above-exposed idea of equitable flux limiting, since the approach will share the flux correction approximately equally between the two variables A and ρ. Note further that the correction coefficients may be such that $\beta_{i,j}^{A,\text{OUT}} \neq \beta_{i,j}^{\rho,\text{OUT}}$; i.e. the resulting procedure is distinct from that suggested in [19].

The correction coefficients (3.11), (3.12) apply to a coupled system of equations consisting of a continuity equation (1.4) and $L = 1$ substance equations of type (1.5). These coefficients will be used in the computational examples in Section 5. In the general case of an arbitrary number L of substance equations, the correction coefficients β appearing in (3.7) are listed in Appendix B as (B10) and (B11).

4. ITERATIVE FLUX-CORRECTION

4.1. *Concept*

It is a general property of flux-correction schemes that the limiting of the fluxes is achieved in a heuristic sense. For instance, the limiting of the incoming fluxes in a particular grid-box is always undertaken by assuming a ''worst-case scenario'' for the outgoing fluxes. This procedure yields a good cost-benefit ratio and a fully satisfactory scheme for many applications. At the same time, however, it is not ''optimal'' in a formal sense. A strict optimization of the flux limiting in a formal sense would indeed require us to evaluate the limiting coefficients by minimizing some functional of the form $\sum (\beta_{i,j}^\rho - 1)^2 + \sum (\beta_{i,j}^{A_l} - 1)^2$ while simultaneously satisfying the conditions (2.3) and (3.5). Such an approach would fully couple the correction-coefficients and, therefore, yield a computationally intensive procedure. As an alternative, we present in this section an iterative technique, which increases the ''accepted'' portion of the higher order fluxes without, however, being optimal in the formal sense exposed above. This new technique is based on the repeated application of the flux-correction, and it is applicable to any type of FCT.

To this end, Eqs. (3.6) and (3.4) are generalized in the sense of

$$\hat{\psi}_{i,j}^{(k+1)} = \hat{\psi}_{i,j}^{(k)} + \tilde{\psi}_{i,j}^{(k)} \tag{4.1}$$

and

$$\tilde{F}_{i+1/2,j}^{(k)\psi_\ell 1} = \beta_{i+1/2,j}^{(k)\psi_\ell 1} F_{i+1/2,j}^{(k)\psi_\ell 1}, \tag{4.2}$$

where k denotes the iteration-step and $\tilde{\psi}^{(k)}$ refers to the divergence of the fluxes $\tilde{\mathbf{F}}^{(k)}$. The start of the iteration is defined by the anti-diffusive fluxes

$$\mathbf{F}^{(0)\psi} = \mathbf{F}^\psi \tag{4.3}$$

and by the first-order approximation

$$\hat{\psi}^{(0)} = \psi^0. \tag{4.4}$$

The first iteration-step constitutes the flux-correction procedure as sketched in Section 3.1. Following this step, the fluxes $\mathbf{F}^{(1)}$ are defined as the remaining fluxes, i.e., the fluxes which were not applied during the previous iteration-step(s). More generally, this takes the form

$$\mathbf{F}^{(k)\psi} = \mathbf{F}^{(k-1)\psi} - \tilde{\mathbf{F}}^{(k-1)\psi}. \tag{4.5}$$

Additional flux-correction steps can now be carried out with the expressions for the correction coefficients, i.e., (3.7), (3.11)–(3.12), but using $\psi^{(k)}$ and $\mathbf{F}^{(k)\psi}$ instead of ψ^0 and $\mathbf{F}^\psi$.

The potential usefulness of this iterative technique derives from the fact that the iteration never decreases the portion of the accepted fluxes and does always possess the desired property of the FCT (e.g., compatibility or monotonicity) at any step k of the iteration. A technical advantage of the iterative application is, furthermore, that it does require only a little additional coding.

A thorough ''experimental'' analysis of the iteration requires the definition of quantities which measure the ''transmitted'' and ''rejected'' portion of the higher-order fluxes. The first such quantity is defined accordingly to

$$\Re^{(k),\psi} = \left\{ \frac{\sum [(F_{i+1/2,j}^{(k+1),1,\psi})^2 + (F_{i,j+1/2}^{(k+1),2,\psi})^2]}{\sum [(F_{i+1/2,j}^{(0),1,\psi})^2 + (F_{i,j+1/2}^{(0),2,\psi})^2]} \right\}^{1/2} \tag{4.6}$$

for each substance ψ, and it measures the relative magnitude of the rejected portion of the ψ-fluxes after the execution of k iteration steps. The sum in (4.6) runs over the whole computational domain such that $\Re$ represents a domain average. Optimal flux-correction should attempt to approach $\Re = 1$, while the rejection of all the fluxes results in $\Re = 0$. Alternatively, the behavior of the kth iteration in accepting the fluxes is evaluated with

$$\tau^{(k),\psi} = 1 - \frac{\Re^{(k),\psi}}{\Re^{(k-1),\psi}}. \quad (4.7)$$

Note that τ measures the effect of the kth iteration alone, rather than the cumulative effect of the preceding iterations as does $\Re$. The quality measures defined in (4.6) and (4.7) will later be evaluated for some numerical examples of Section 5.

4.2. *One-Dimensional Advection Test*

It is well known that flux correction can introduce certain pathological behaviors. This is particularly obvious in some examples which would not require any flux correction, such as the advection of smooth anomalies. An example is shown in Fig. 4. It illustrates the advection of a sinusoidal distribution with the Lax–Wendroff scheme. The numerical resolution in the periodic domain $[-0.5, 0.5]$ is set to $\Delta x = 0.025$, and we consider advection with velocity 1 during 100 time units and with Courant number 0.5 (corresponding to 8000 time-steps). Panel (a) illustrates the analytical solution, while panel (b) presents the Lax–Wendroff solution without flux correction. It can be observed that there is a significant phase error, which has accumulated over the long integration time, but the amplitude and the shape of the sine curve are rather well preserved. Panel (c) shows the results of the same test but with the Lax–Wendroff scheme enhanced by the traditional FCT procedure [36]. Several major deficiencies are apparent. There is a drastic reduction in amplitude, and the symmetry of the sine curve is seriously distorted.

These errors are reduced drastically when using the iterative flux-correction procedure with two iteration steps (panel d). For the numerical example in this latter panel the procedure outlined in Section 4.1 is followed. The first of the two iteration steps corresponds to the traditional flux limiting. In the second step, the fractions of the higher order fluxes which were rejected during the first iteration are computed from (4.5) and corrected using the same traditional FCT procedure as in the first step. As can be seen from Fig. 4d, this second iteration restores the amplitude of the numerical solution towards its analytical counterpart. The gain in amplitude is more than 100%, and the asymmetries are almost completely removed (compare with Fig. 4c). There is still some slight loss in amplitude when comparing to the plain Lax–Wendroff solution (Fig. 4b), but at the same time the phase error is slightly reduced. It follows that most of the behavioral error evident in Fig. 4c is the result of unjustifiably rejecting some portion of the higher order fluxes.

It is important to note that the iterative application of FCT always preserves the beneficial aspects of the original formulation. This is illustrated in Fig. 5 which shows a similar advection test but with a step-like anomaly that is advected during one time unit. In this case, the plain Lax–Wendroff scheme produces spurious under- and overshoots (panel b), which are suppressed by either traditional or iterative flux-correction (panel c and d). In this particular example the effect of the iterative flux correction is weak and not visible in the diagrams.

In summary, the two examples demonstrate that the iterative application of flux correction does drastically reduce some pathological aspects of FCT, while fully retaining the benefits.

4.3. *Application to the Compatible Transport Formalism*

As illustrated above, iterative flux correction can be beneficial, even in the context of traditional limiters. It is, however, likely to be more important in synchronous flux correction, where complex limiting constraints can lead to the ''unjustified'' rejection of a substantial fraction of the higher order fluxes. Here we discuss how the iterative procedure can be applied to the compatible transport scheme designed in Section 3, but consideration is given also to the coupling of the latter limiting to traditional flux corrections.

With the implementation of the compatibility constraint (2.3) onto the mixing ratios $a_l = \rho/A_l$, there is no formal guarantee that any of the primary variables ρ and A_l behaves nonoscillatory. It is therefore desirable to couple the synchronous flux limiting to other flux-correction procedures. Such an attempt is straightforward, since the classical flux corrections can be applied to the individual fields prior to feeding the fluxes into the synchronous flux-correction procedure described in Section 3. With this generalization, the synchronous and iterative flux-correction code comprehends the following steps:

(i) compute first-order time step $\psi^{0,n+1}$ and higher order fluxes,

(ii) apply classical flux correction to higher order fluxes (optional),

(iii) compute the bounds (2.4) based on data from time-level n,

(iv) compute the divergence of incoming and outgoing higher order fluxes for all the fields according to (B2),

(v) compute the correction coefficients with (3.11), (3.12),

(vi) carry out flux-correction step according to (3.7),

(vii) compute flux divergence of corrected fluxes and update the first-order estimate to the flux-corrected higher order estimate,

(viii) compute ''rejected'' fluxes with (4.5) and proceed with next iteration step at (iv).

In the sequence above, only the synchronous flux correction is iterated. An alternative sequence could be con-

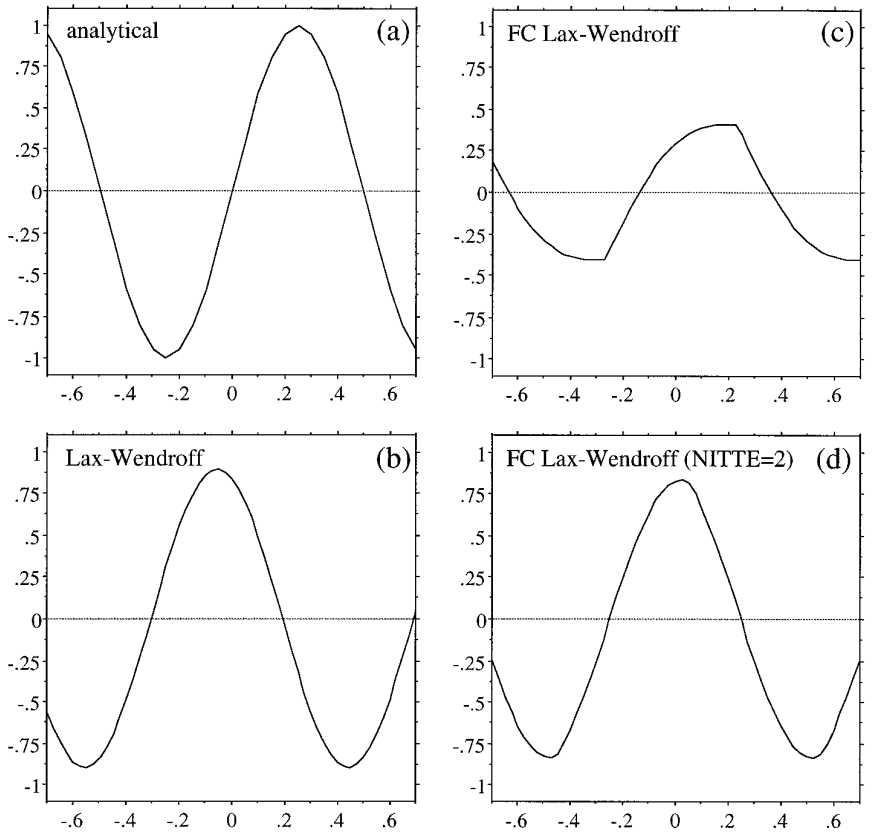

FIG. 4. One-dimensional advection of a sinusoidal anomaly with Courant number 0.5 in the periodic domain $[-0.5, 0.5]$. The advective velocity is 1 and the integration time is 100. The panels show (a) the analytical solution, (b) the numerical Lax–Wendroff solution, (c) the traditional flux-corrected Lax–Wendroff solution, and (d) the Lax–Wendroff solution with two iterative flux-correction steps.

structed by treating the traditional flux correction within the iterative loop as well. Some tests have, however, indicated that the resulting gain is small, presumably since the dominating flux correction is often the compatible rather than the traditional one.

5. TESTS AND COMPUTATIONAL EXAMPLES

5.1. *Application to the Deformation Test*

We now briefly return to the deformation test introduced in Section 2.2. Figure 6 shows the results when the synchronous flux-correction technique is employed with two iterative steps. The underlying schemes used for the generation of the second-order fluxes are again the MPDATA-scheme (Fig. 6a) and the Lax–Wendroff scheme (Fig. 6b). For comparison with other flux-correction schemes the right-hand panels should be compared with Fig. 3.

The results demonstrate how the synchronous flux correction successfully restores compatibility for both the schemes. The predicted mixing ratio $a = A/\rho$ now fully satisfies (2.11) and (2.3), which was not the case for classical flux correction (cf. Fig. 3), even when synchronized according to [19]. The price to pay is a slight loss in the amplitude of some of the finer scale features in ρ and A. This loss is, however, comparable to that associated with Löhner synchronization (cf. Fig. 3b): In the case of the plain MPDATA-scheme, the maximum of the A variable at time $t = 1$ is $A_{\max}\ \mathrm{e}^{-1} = 0.694$. The respective values for the synchronization according to [19] and according to Section 3 are $A_{\max}\ \mathrm{e}^{-1} = 0.615$ and $A_{\max}\ \mathrm{e}^{-1} = 0.616$, respectively. These values are significantly above $A_{\max}\ \mathrm{e}^{-1} = 0.524$, obtained with the first-order upstream scheme.

From a physical point of view, the mixing ratio becomes ill-defined at locations with zero density. In our analytical solution this happens at $|x|e^t > 1$. In a numerical approximation, however, $\rho = 0$ is only approximately realized, and the mixing ratio remains well defined at locations where its analytical counterpart is not. At these locations the appropriate value of the mixing ratio can be inferred from physical arguments: The mass at $|x|e^t > 1$ is the result of (implicit) numerical diffusion, and it must have originated from $|x|e^t \approx 1$. This implies that it must have the properties of the mass originally located at $|x| \approx 1$, i.e., $a = 1$. The tendency to produce this value for $|x| > 1$ can be identified

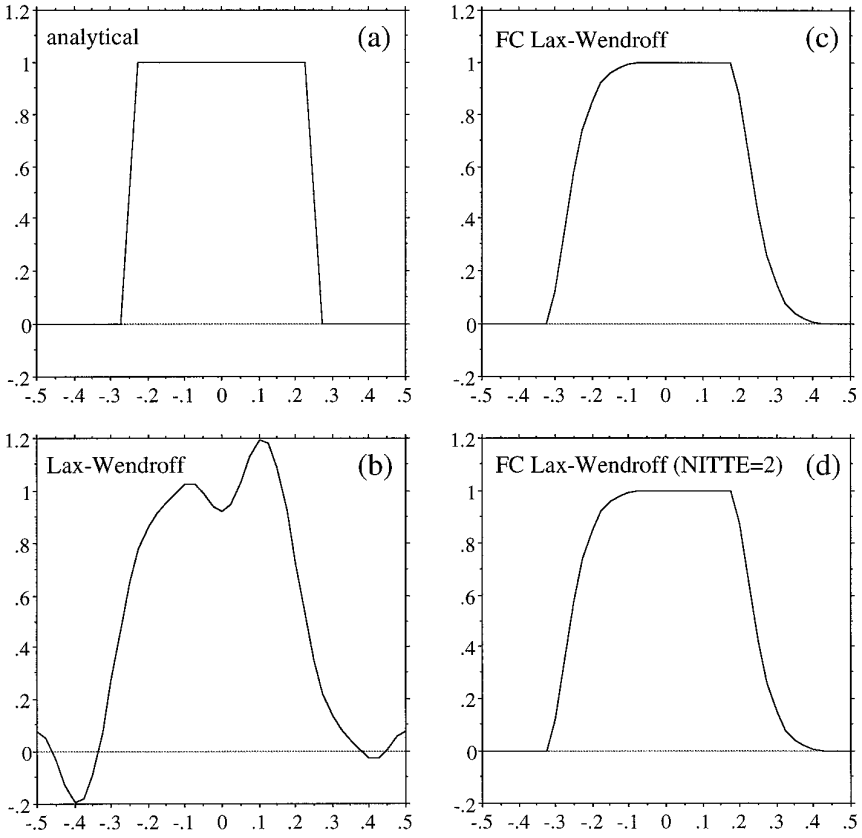

FIG. 5. As Fig. 4 but for a step function and integration time 1.

in the diagrams for the upstream as well as the MPDATA scheme (cf. Fig. 2 and Fig. 3) and is clearly evident in the flux-corrected results of Fig. 6. This physically consistent behavior directly derives from the proper implementation of compatibility as defined in Section 2.1.

5.2. *Spreading of a Drop of Shallow Water*

The shallow water equations are closely related to the compressible flow equations, and they can also serve as a framework to test numerical concepts related to hydrostatic geophysical flow problems with material vertical coordinates. This includes, in particular, vertical discretizations based upon isentropic surfaces (constant potential temperature), or isosteric and isopycnic surfaces (constant density). Atmospheric and oceanic numerical models of this type have a long history. An overview and a succinct account of key numerical issues can be found in Bleck [3]. For some more recent material the reader is referred to [4, 1, 23].

If the computational surfaces in these models intersect with the underlying topography (or with each other), they can numerically be represented as partially collapsed [2]. This is an attractive strategy as it avoids the explicit tracking of the intersections, but it also introduces notable numerical difficulties associated with the large relative variations of the layer-depth variable near the intersections. In particular, in conservative formulations the velocity must be diagnosed from the momentum and layer-depth variables by a division, and this division becomes ill-defined in the collapsed layers. This issue requires highly consistent (or compatible) fields near the intersection, where both layer depth and momentum must simultaneously tend to zero with their ratio always being well defined. With incompatible time-stepping procedures, the diagnosis of the velocity variable can easily yield infinite velocities, which will immediately terminate the integration through the violation of the CFL-criterion.

Here a related numerical test is presented within the framework of the one-dimensional shallow-water (or shallow-fluid flow) equations. The test is based on an analytical solution, and its purpose is to demonstrate how the proposed synchronous flux correction is able to correctly handle collapsed surfaces in models with material vertical coordinates. In dimensionless notation, the governing equations, in absence of surface friction and background rotation can be expressed as (see [25])

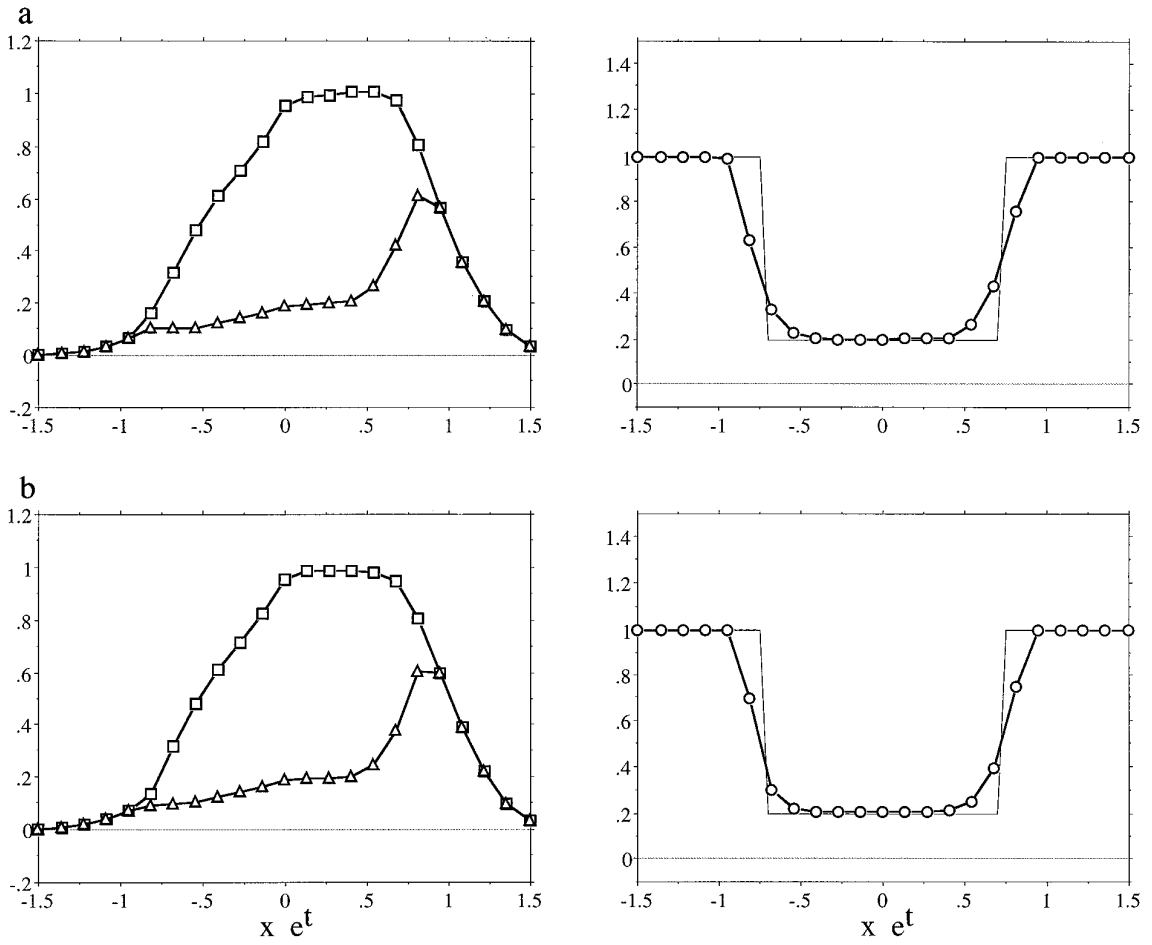

FIG. 6. As Fig. 2, but with application of the compatible synchronization technique with NITTE = 2 iterations. The underlying schemes are (a) the second-order MPDATA scheme and (b) the Lax–Wendroff scheme.

$$\frac{\partial Hu}{\partial t} + \frac{\partial (uHu)}{\partial x} = -H\frac{\partial H}{\partial x}, \tag{5.1}$$

$$\frac{\partial H}{\partial t} + \frac{\partial (uH)}{\partial x} = 0, \tag{5.2}$$

where u is the velocity in the x-direction, and H is the depth of the fluid layer. We consider the spreading of a parabola-shaped two-dimensional drop of shallow water on a horizontal plane. The drop is initially confined to $|x| \leq 1$ according to

$$H(x, t=0) = \begin{cases} 1 - x^2 & \text{for } |x| \leq 1 \\ 0 & \text{for } |x| \geq 1 \end{cases} \tag{5.3}$$

and at rest. Upon releasing the drop, it spreads under the effect of gravity. The temporal evolution of this system has been analytically investigated by Frei [9]. He noted that the parabola shape is always retained and that the velocity across the drop is a linear function of x. In our case, the dimensionless solution can be represented by

$$H(x, t) = \lambda^{-1}[1 - (x/\lambda)^2] \tag{5.4}$$

$$u(x, t) = x(\lambda_t/\lambda), \tag{5.5}$$

where λ describes the half-width of the drop, and $\lambda_t = \partial\lambda/\partial t$ is the velocity of the leading edge. Following [9], the function $\lambda(t)$ is obtained numerically as the root of the equation

$$t = \tfrac{1}{2}[\sqrt{\lambda(\lambda - 1)} + \ln(\sqrt{\lambda - 1} + \sqrt{\lambda})] \tag{5.6}$$

and

$$\lambda_t = 2\sqrt{1 - \lambda^{-1}}. \tag{5.7}$$

The analytical solutions for $t = 0$, 1, 2, and 3 are shown in Fig. 7a. They represent an excellent test case for numerical

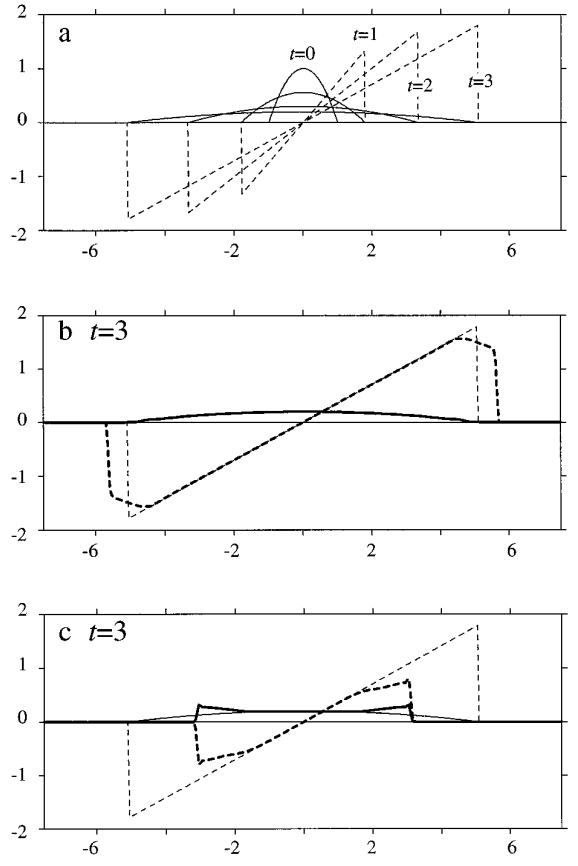

FIG. 7. The spreading drop test. A parabola-shaped drop of shallow water is released from rest on an underlying surface and spreads under the effect of gravity. Panel (a) shows the analytical solution according to [9] at = 0, 1, 2, and 3. Full and dashed lines show the free surface of the drop and the velocity, respectively. Panel (b) shows the numerical results at time $t = 3$ obtained with the use of the synchronization technique developed in this paper. For comparison, an integration based on a non-conservative advective formulation is shown in (c). The thin lines in (b) and (c) show the analytical solution for comparison.

schemes. There is a moving intersection and, as the drop spreads with increasing velocity, a wide range of Courant numbers is encountered.

Here two experiments with both a conservative and a non-conservative numerical formulation are tested. Both the formulations employ zero-explicit diffusion, and the right-hand side of (5.1) is evaluated using second-order-accurate differencing in time and space following [33] (technically, this reduces to advecting momentum plus half of its forcing, times Δt, and adding half of the new forcing, times Δt, afterwards). The resolution is $\Delta x = 0.05$ and $\Delta t = 0.01$. The rationales for comparing conservative and non-conservative algorithms will become clear later in this section.

In the first numerical formulation, the left-hand side of (5.1)–(5.2) is implemented by using the synchronous flux correction technique of Section 3 with NITTE = 2 iterations. The underlying higher-order fluxes are obtained from the second-order MPDATA scheme (IORD = 2). The results (Fig. 7b) are in excellent agreement with the analytical solution (thin lines). There are some notable differences in the velocity field at the thin layer near the leading edge of the spreading drop, but this is of minor concern since there is little momentum associated with it, and since the velocity remains properly bounded.

The second numerical experiment is based upon the advective form of the momentum equation, i.e.,

$$\frac{\partial u}{\partial t} + u\frac{\partial u}{\partial x} = -\frac{\partial H}{\partial x}. \tag{5.8}$$

The left-hand side of (5.8), (5.2) is integrated using the second-order MPDATA scheme (with IORD = 2 and without any flux correction), and the forcing term on the right-hand side is treated similarly to the conservative scheme discussed above (since MPDATA is inherently a flux-form algorithm, the second term on the left-hand side is viewed as $0.5\partial u^2/\partial x$). The results (Fig. 7c) show the formation of shock-like structures at the leading edge of the drop, in stark contrast with the analytical solution. This erroneous behavior cannot be corrected for by higher resolution; i.e., the scheme does not converge. This kind of pathological behavior appears to be typical for a wide range of numerical schemes based upon the advective form of the equations and has also been documented in the literature by Hartjenstein and Egger [16].

It is well known that the use of non-conservative numerical techniques can lead to seriously biased results whenever shocks or strong dissipation occur. The spreading-drop test illustrated above is an example of a flow which is fully inviscid (cf. its analytical solution) but, nevertheless, prone to serious deficiencies when integrated with a non-conservative scheme. The apparent inability of the advective formulation to describe the progression of the leading edge of the drop results from the violation of momentum conservation. Consistent with this interpretation, advective numerical formulations can be complemented with an explicit momentum-conservative pseudo-viscosity term of the form discussed by [4, 25, 10]. The correct solution to the spreading drop test can then be recovered. However, in order for this approach to yield satisfactory results, the explicit dissipation of the scheme must be strong enough to clearly overpower the false violation of momentum conservation inherent to the scheme itself. Such a formulation is hence overly diffusive.

Although the results in Fig. 7 clearly indicate that the conservative formulation is superior for the problem at hand, most geophysical models of isentropic/isopycnic formulations use some advective form of the equations which does not guarantee momentum conservation (see [1–4, 16],

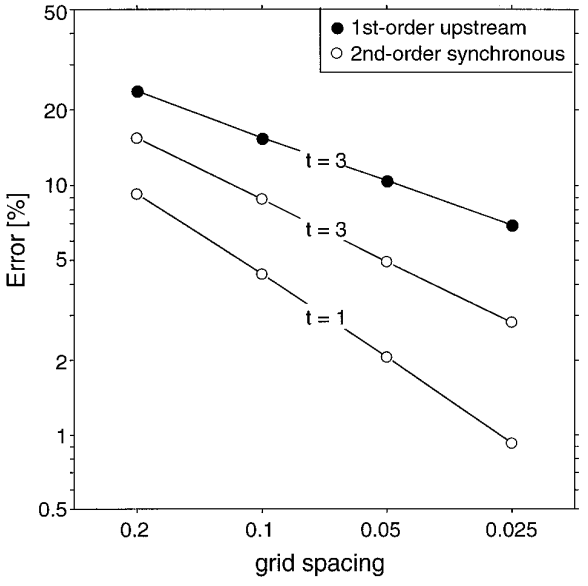

FIG. 8. Error measure (5.9) as a function of grid spacing. Empty and full symbols are for a formulation based on the second-order synchronous flux correction with NITTE = 2 iterations (cf. Fig. 7b) and for the first-order upstream scheme, respectively.

but see also [23]). We believe that this tradition is related to the difficulties in obtaining stable integrations based upon the conservative form of the equations. In conservative formulations, the use of incompatible schemes for the transport of mass and momentum can produce excessive velocities near intersections of fluid surfaces with the underlying terrain. With respect to the spreading-drop test, we have observed that several higher order schemes are unstable as a result of such incompatibilities. Examples include the Lax–Wendroff scheme (with or without traditional flux correction) and combinations of different schemes for the transport of mass and momentum. On the other hand, schemes which are fully or almost compatible (such as the upstream and the MPDATA scheme; see Appendix A and Section 2.2) yield results similar to those shown in Fig. 7b.

One purpose of the synchronous flux correction proposed in this paper is to correct the higher order fluxes of an arbitrary scheme (or an arbitrary combination of schemes) such that the resulting fluxes yield compatible results. For isentropic, isopycnic, and shallow-water equations, this feature guarantees that the velocity variable remains bounded, which in turn yields attractive stability properties of the algorithm.

Some indication of the convergence of the synchronous flux correction technique is presented in Fig. 8, where an error measure in terms of

$$E_{\text{mom}} = \left[\frac{\sum \left[(Hu)_{\text{num}} - (Hu)_{\text{ana}} \right]^2}{\sum \left[(Hu)_{\text{ana}} \right]^2} \right]^{1/2} \tag{5.9}$$

is displayed as a function of grid distance. Here the subscripts refer to numerical and analytical solutions, and the summation runs over all the grid-points. The corresponding term for the mass variable shows similar characteristics and is not further discussed. For reference, Fig. 8 also displays the errors associated with a first-order numerical formulation based upon the upstream scheme. At $t = 3$, the convergence of the former algorithm is merely 58% faster, but the overall error of the latter scheme exceeds that of the second-order formulation by 62% to 148% (depending on the resolution). The third curve in Fig. 8 also shows that the convergence rate at $t = 1$ is substantially faster than at $t = 3$. Note, however, that the convergence rate cannot be directly related to the order of accuracy of the scheme, since the underlying flow solution is discontinuous. Thus the mere statement of the improved convergence with the higher order scheme is encouraging.

5.3. *Two-Dimensional Hydrostatic Flow Past a Ridge*

As a last computational example, consideration is given to the flow of an incompressible, non-rotating, density-stratified Boussinesq fluid past a two-dimensional mountain ridge. The system of equations is cast in isosteric coordinates (cf. [27, 29]) and then takes on the form

$$\frac{\partial U}{\partial t} + \frac{\partial (uU)}{\partial x} = -\frac{\partial p}{\partial \alpha}\frac{\partial M}{\partial x}, \tag{5.10}$$

$$\frac{\partial}{\partial t}\left(\frac{\partial p}{\partial \alpha}\right) + \frac{\partial}{\partial x}\left(u\frac{\partial p}{\partial \alpha}\right) = 0. \tag{5.11}$$

Here $\alpha = \rho^{-1}$ is the specific volume vertical coordinate of the model, ρ is the pressure, $U = u(\partial p/\partial \alpha)$ is horizontal momentum, and $M = \alpha p + gh$ is the Montgomery potential with h and g denoting the actual height of a density surface and the acceleration of gravity, respectively. The prognostic equations for momentum and mass continuity (5.10)–(5.11) are supplemented with the diagnostic relationship for the hydrostatic balance of the fluid, i.e.,

$$\frac{\partial M}{\partial \alpha} = p. \tag{5.12}$$

The upper boundary condition incorporates the free surface assumption ($p = \text{const}_{\alpha \to \infty}$), whereas for the lower boundary a material surface with a free-slip boundary condition is assumed.

The numerical implementation of the system involves a regular mesh in (x, α), the quasi-horizontal transport of the layer-thickness $(\partial p/\partial \alpha)$, and the momentum-variable U, according to (5.10)–(5.11), a discretization of the pressure forcing term according to [33], the recovery of the velocity from the momentum variable, and finally, the ver-

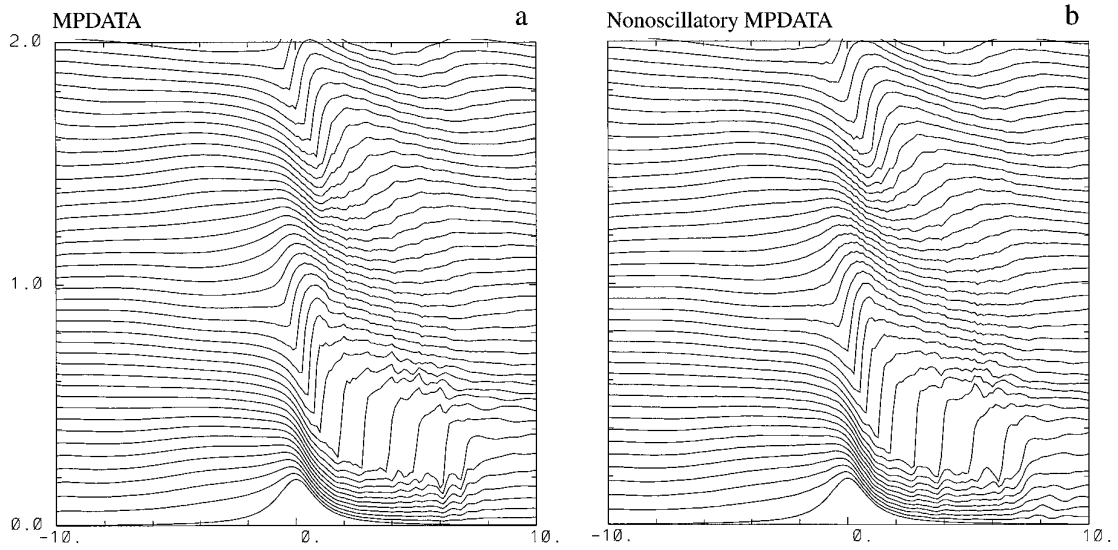

FIG. 9. Vertical section showing the distribution of computational surfaces (corresponding to density surfaces, or isosteres) in stratified hydrostatic flow past a two-dimensional ridge. The flow is from left to right. The underlying numerical transport scheme for these solutions are (a) the MPDATA algorithm without flux correction and (b) the same algorithm but with traditional flux correction [31].

tical integration of (5.12). To simulate an infinite extent of the fluid, a gravity-wave absorber [17] is employed in the upper third of the model domain, and relaxation at the inflow and outflow boundaries [8]. These latter regions are excluded from the diagrams to be shown below. There is zero explicit dissipation in the formulation. Some further details of the model are described in [29].

The current experimental setup assumes uniform upstream profiles of $u_0 = 20$ ms^{-1}, a constant Brunt–Väisälä frequency $N = 2.094 \times 10^{-2}$ s^{-1}, and a bell-shaped hill

$$h(x) = H[1 + (x/L)^2]^{-1} \tag{5.13}$$

with a horizontal scale $L = 12000$ m and height $H = 1146$ m. These flow parameters, characteristic of the downslope windstorm regime, were selected accordingly to [21, 29]. The computational domain covers 22 L and 3 λ, where $\lambda = 2\pi U/N$ denotes the vertical wavelength of hydrostatic gravity waves. The computational resolution is 176 grid intervals in the horizontal, 61 isosteric levels initially spaced at 300-m intervals, and the time-step is 6 s. Results will be shown after 2400 time-steps, corresponding to 24 characteristic time scales, $T = L/u_0$.

Here we give examples and discuss the effect of various transport schemes on the evolution of the flow. Figure 9a shows the numerical results using the MPDATA scheme for the transport of the density and momentum variable. After the flow is impulsively started from rest, a pattern of vertically propagating gravity waves is established, which leads to the formation of a downslope windstorm (evident from the almost collapsed density surfaces over the lee slope) and to the onset of gravity wave breaking (manifesting itself in the neutrally stratified region aloft). The explicit representation of the wave-breaking process would require the consideration of the non-hydrostatic dynamics in conjunction with some turbulence parameterization (see, e.g., [21]). In our case the dissipation is accomplished with the implicit diffusion inherent to the transport scheme, instead, and the approximate hydrostatic solution in Fig. 9a is qualitatively correct (compare with the corresponding non-hydrostatic results published in [21]).

The solution obtained in the above way is quite noisy, and it proves difficult to achieve smooth and accurate solutions. The oscillations in Fig. 9a are the result of the nonlinear coupling between equations (5.10)–(5.12), and cannot simply be removed by supplementing the transport algorithm with classical flux correction (see Fig. 9b). Smooth solution can be obtained with the first-order upstream scheme, but this results in a significant under-estimation of the upper-level gravity wave signal as a result of excessive diffusion. Furthermore, as discussed in [29], adding some weak diffusion to the momentum equation (or using the first-order upstream scheme) results in a drastic underestimation of the neutrally stratified region which separates the high-speed shooting flow near the surface from the flow aloft. These results indicate that the solution is highly dependent upon the way how dissipation is numerically represented.

Figure 10 presents the results when applying the synchronous and compatible flux-correction technique to the transport of the prognostic variables U and $(\partial p/\partial \alpha)$. The two panels show the results for NITTE = 1 and 2 iterations.

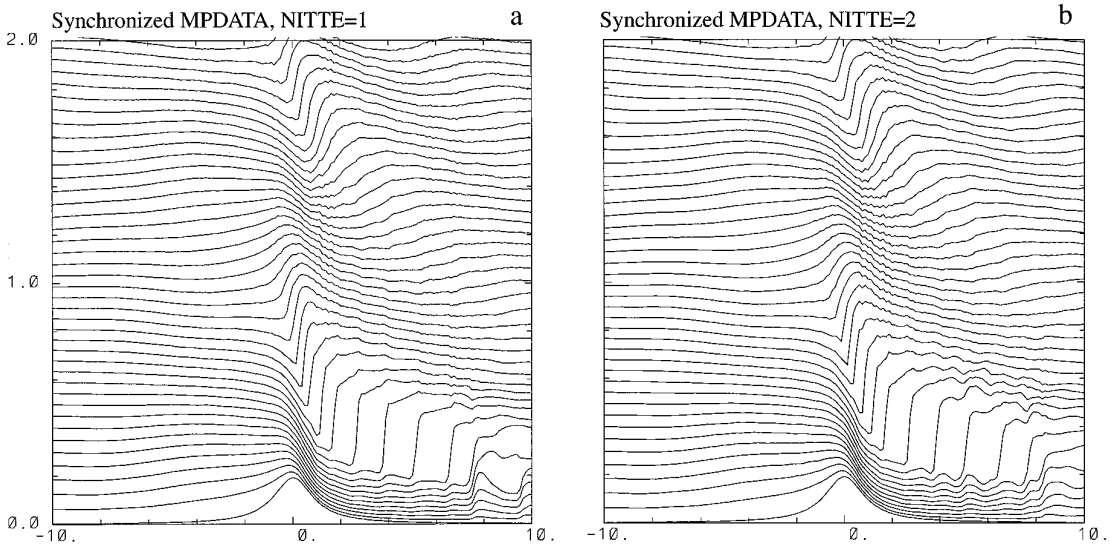

FIG. 10. As Fig. 9, but using the synchronous and compatible flux correction for the transport of mass and momentum. The two panels are based upon flux-correction with (a) one iteration and (b) two iterations.

Both the integrations yield a fairly smooth and accurate solution, indicating that the implementation of the physically based compatibility constraint helps in mimicking dissipation effects.

In order to further demonstrate the improvement of the solution through iterative flux correction, we display in Fig. 11 the objective quality measures earlier defined in Section 4. The respective numerical simulation is identical to those shown in Fig. 10, except for using NITTE = 4 iterations. At every timestep, (4.6)–(4.7) was monitored for all iteration steps, and the averaged results over the whole integration are shown in Fig. 11. Panel (a) presents the portion of the second-order fluxes which is rejected after k iterations. Likewise, panel (b) shows the portion of the fluxes transmitted in the kth iteration step. The two curves in the figure relate to the equations of mass and x-momentum. It can be observed that the "transmission rates" (panel b) are around 70% in the first iteration step, between 50% and 60% in the second iteration step, and subsequently drop to a few percent. At the same time the overall rejection rate appears to converge to values near 15% (panel a). In our example the iteration essentially converges in two steps. This rapid convergence is, however, not a universal property of the proposed scheme. For two-dimensional shallow-water flow past isolated topography (discussed in [25,

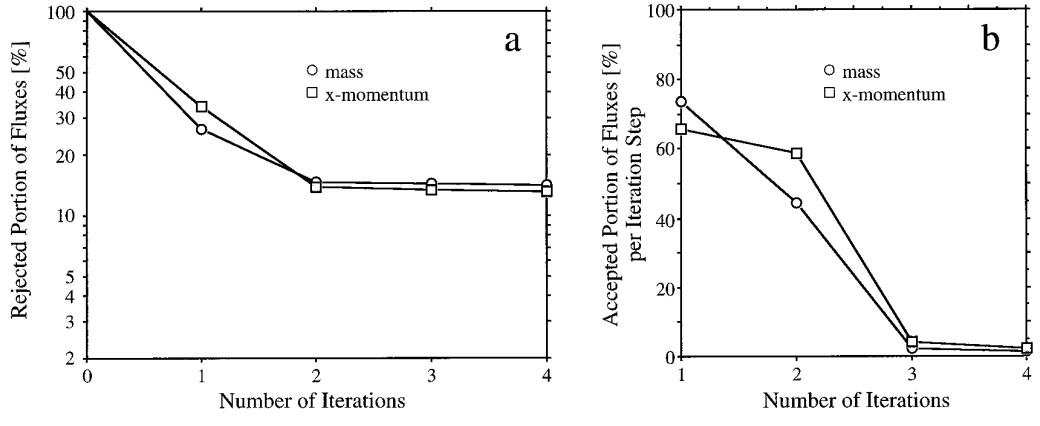

FIG. 11. Effectiveness of iterative synchronous flux correction for a simulation similar to those in Fig. 10, but using NITTE = 4 iteration steps. Panel (a) shows the "rejected" portion of the higher order fluxes after 1, 2, 3, and 4 iteration-steps, and panel (b) shows the "transmitted" portion of the fluxes as a function of the iteration step. The two curves relate to the higher order fluxes associated with the transport of mass and the momentum.

26, 13]), we have observed that the convergence requires three to four iteration steps.

6. CONCLUDING REMARKS

In this paper consideration was given to the coupled transport of density and additional conserved quantities according to (1.4)–(1.5). For this case, a synchronous and iterative flux correction technique was developed which ensures that the mixing ratios $a_l = A_l/\rho$ behave in accordance with the Lagrangian form of the transport equation. This property of a scheme is referred to as compatibility. In the current paper we have studied the case in the absence of sources and sinks. In this case ''natural'' limiters do derive from the compatibility constraint, and the flux correction can be achieved without resorting to bounds derived from a first-order time-step.

If coupled transport equations (1.2)–(1.3), including source terms $\mathbf{R} \neq 0$ are considered, the formalism might be generalized using the advective form of (1.3), viz.,

$$\frac{d}{dt}\left(\frac{V_l}{\rho}\right) = \frac{R_l}{\rho}, \tag{6.1}$$

which could serve as the basis for a generalized algorithm. Following the treatment in classical FCT, the procedure could involve a first-order estimate of (6.1), and generalized bounds in (2.3) could then be obtained using predictor–corrector ideas. This procedure collapses to (2.4) in the case of $\mathbf{R} = 0$ and is left for future research.

Another aspect considered in this study is the iterative application of flux corrections. This procedure does help to reduce the portion of the rejected anti-diffusive fluxes, and it was demonstrated that it helps in reducing the behavioral errors of traditional FCT schemes.

The synchronous and iterative flux correction algorithm is not overly expensive (i.e., about twice the cost of transporting the substances with classical FCT), but it can be in conflict with the programming structure of complicated codes since it requires the simultaneous transport of the variables. Nevertheless the new technique appears useful for various flow problems. In relation to the transport of density and momentum, the issue of compatibility is particularly germane to fluids with large density variations, as they occur in some combustion problems and in situations where a fluid is released into a low density environment or into the vacuum. Compatibility between density and momentum can also become a crucial issue in isentropic, isosteric, and isopycnic formulations of hydrostatic fluids with small density variations.

APPENDIX A: COMPATIBILITY OF THE UPSTREAM SCHEME

In this appendix it is shown that the upstream scheme is compatible. For simplicity the proof is carried out for the one-dimensional case with one substance, but the generalization to the full proof is straightforward. Consider the transport of ρ and an additional substance A, i.e.,

$$\frac{\partial \rho}{\partial t} + \frac{\partial}{\partial x}(u\rho) = 0, \tag{A1a}$$

$$\frac{\partial A}{\partial t} + \frac{\partial}{\partial x}(uA) = 0, \tag{A1b}$$

to be accomplished with the sign-preserving and linear upstream scheme. The latter can be cast into the form

$$\rho_i^{n+1} = \sum_{j=-1}^{1} c_{i,j}\rho_{i+j}^n, \tag{A2a}$$

$$A_i^{n+1} = \sum_{j=-1}^{1} c_{i,j}A_{i+j}^n. \tag{A2b}$$

The linearity of the scheme implies that the c-coefficients do not depend on the transported field, but on the velocity-field alone; i.e., the same coefficients appear in (A2a) and (A2b). In order to be sign-preserving (for an arbitrary functional shape of a non-negative ρ), the c-coefficients in (A2) must, in addition, be positive. The effects of (A2) on the mixing ratio $a = A/\rho$ are obtained after dividing (A2b) by (A2a). This yields

$$a_i^{n+1} = \sum_{j=-1}^{1} d_{i,j}^n a_{i+j}^n \tag{A3}$$

with

$$d_{i,j}^n = c_{i,j}\rho_{i+j}^n \left(\sum_{j=-1}^{1} c_{i,j}\rho_{i+j}^n\right)^{-1} \quad \text{for } j = -1 \text{ to } 1. \tag{A4}$$

It can be verified that

$$\sum_{j=-1}^{1} d_{i,j}^n = 1. \tag{A5}$$

Together with $d_{i,j}^n \geq 0$, this implies that (A3) simply expresses the mixing ratio a_i^{n+1} at time-level $n+1$ as some weighted average of a_{i-1}^n, a_i^n, and a_{i+1}^n at time-level n. It follows that the one-dimensional scheme under consideration is compatible, i.e.,

$$\min(a_{i-1}^n, a_i^n, a_{i+1}^n) \leq a_i^{n+1} \leq \max(a_{i-1}^n, a_i^n, a_{i+1}^n). \tag{A6}$$

This proof can easily be generalized to multi-dimensional geometry and to the case of several substances. In addition, it can be generalized to an arbitrary linear, positive definite finite-difference scheme with forward time-stepping.

It is worth noting that the compatibility of the upstream scheme even holds in the presence of massless gridpoints and, in the strict sense, as outlined in the last paragraph of Section 2.1. This follows upon noting that

$$d^n_{i,j} a^n_{i+j} = c_{i,j} A^n_{i+j} \left(\sum_{j=-1}^{1} c_{i,j} \rho^n_{i+j} \right)^{-1}$$

and the contribution of a massless gridpoint (with $A = \rho = 0$) to a^{n+1}_i in (A3) is zero.

APPENDIX B: DERIVATION OF THE CORRECTION COEFFICIENTS

Here the correction coefficients $\beta^{A,\mathrm{OUT}}$, $\beta^{A,\mathrm{IN}}$, $\beta^{\rho,\mathrm{OUT}}$, and $\beta^{\rho,\mathrm{IN}}$ are derived for the situation discussed in Section 3. First the case of a coupled system of Eqs. (1.4), (1.5) with $L = 1$ substance will be treated. For brevity we will also assume two-dimensional geometry, but the generalization to arbitrary dimensions is straightforward.

(a) *Density and One Additional Conserved Substance*

We start by splitting the second-order corrections $A'_{i,j}$ and $\rho'_{i,j}$ appearing in (3.6) into contributions arising from in- and out-coming fluxes, i.e.,

$$\psi'_{i,j} = \psi^{\mathrm{in}}_{i,j} + \psi^{\mathrm{out}}_{i,j}, \tag{B1}$$

where the symbol ψ stands for A or ρ and where

$$\psi^{\mathrm{in}}_{i,j} = (F^{\psi,1}_{i-1/2,j})^+ - (F^{\psi,1}_{i+1/2,j})^- + (F^{\psi,2}_{i,j-1/2})^+ - (F^{\psi,2}_{i,j+1/2})^-, \tag{B2a}$$

$$\psi^{\mathrm{out}}_{i,j} = (F^{\psi,1}_{i-1/2,j})^- - (F^{\psi,1}_{i+1/2,j})^+ + (F^{\psi,2}_{i,j-1/2})^- - (F^{\psi,2}_{i,j+1/2})^+. \tag{B2b}$$

Here the lower-case superscripts "in" and "out" must be distinguished from the upper-case superscripts appearing in (3.7). The two contributions satisfy $\psi^{\mathrm{in}}_{i,j} \geq 0$ and $\psi^{\mathrm{out}}_{i,j} \leq 0$ and thus, as follows from (B1), provide bounds for $\tilde{A}$ and $\tilde{\rho}$ for any type of flux correction, i.e.,

$$\psi^{\mathrm{out}}_{i,j} \leq \tilde{\psi}' \leq \psi^{\mathrm{in}}_{i,j}. \tag{B3}$$

Upon introducing the specific form (3.7) of the anticipated flux correction into (B3) one obtains

$$\beta^{\psi,\mathrm{OUT}}_{i,j} \psi^{\mathrm{out}}_{i,j} \leq \tilde{\psi}' \leq \beta^{\psi,\mathrm{IN}}_{i,j} \psi^{\mathrm{in}}_{i,j}. \tag{B4}$$

In essence, these bounds are based on a worst-case scenario. For instance, the smallest values of $\tilde{\psi}'$ are realized when the incoming fluxes $\psi^{\mathrm{in}}_{i,j}$ are reduced to zero while the outgoing fluxes are left unchanged by the correction.

The bounds given by (B4) are next utilized in order to derive explicit expressions for the limiting coefficients β such as to satisfy the compatibility relation (2.3). For this analysis a case distinction is employed. Consider first equation (3.10a) with $a^{\min}_{i,j} \geq 0$. Introducing (B4) into (3.10a) yields

$$a^{\min}_{i,j} \rho^0_{i,j} - A^0_{i,j} \leq \beta^{A,\mathrm{OUT}}_{i,j} A^{\mathrm{out}}_{i,j} - a^{\min}_{i,j} \beta^{\rho,\mathrm{IN}}_{i,j} \rho^{\mathrm{in}}_{i,j}. \tag{B5}$$

This is a sufficient condition which can, in principle, be met by a range of choices for $\beta^{\rho,\mathrm{IN}}_{i,j}$ and $\beta^{A,\mathrm{OUT}}_{i,j}$. Recalling that we are considering the case with $a^{\min}_{i,j} \geq 0$, we stipulate that these two coefficients should satisfy

$$\beta^{\rho,\mathrm{IN}}_{i,j} \leq \beta^{A,\mathrm{OUT}}_{i,j}. \tag{B6}$$

As can be verified a posteriori, this stipulation yields an equitable distribution of the flux correction onto the two variables. Introducing (B6) into (B5) yields

$$a^{\min}_{i,j} \rho^0_{i,j} - A^0_{i,j} \leq \beta^{A,\mathrm{OUT}}_{i,j} [A^{\mathrm{out}}_{i,j} - a^{\min}_{i,j} \rho^{\mathrm{in}}_{i,j}] \tag{B7}$$

and an upper bound for $\beta^{A,\mathrm{OUT}}_{i,j}$ is obtained as

$$\beta^{A,\mathrm{OUT}}_{i,j} \leq \frac{a^{\min}_{i,j} \rho^0_{i,j} - A^0_{i,j}}{A^{\mathrm{out}}_{i,j} - a^{\min}_{i,j} \rho^{\mathrm{in}}_{i,j} - \varepsilon}, \tag{B8}$$

where a small number ε (e.g., $\varepsilon = 10^{-20}$) has been introduced into the denominator for computational efficiency. In deriving (B8), we did use knowledge of the sign of the individual terms. For instance, from the fact that the low-order approximation satisfies the compatibility relation (2.3) we have

$$a^{\min}_{i,j} \leq (A^0/\rho^0)_{i,j} \leq a^{\max}_{i,j}, \tag{B9}$$

and with $a^{\min}_{i,j} \geq 0$, as assumed above, it follows that the numerator of (B8) is negative. Similarly, all the individual terms contributing to the denominator are negative as well.

The preceding analysis has to be performed for Eq. (3.10a) and both signs of $a^{\min}_{i,j}$, as well as for Eq. (3.10b) and both signs of $a^{\max}_{i,j}$. The results of these four cases are listed in Table I. In order to avoid the computationally costly case distinctions in the table, the correction coefficients can efficiently be summarized, as given by (3.11) and (3.12) in the main text.

(b) *Density and an Arbitrary Number of Conserved Substances*

The generalization to the case of a mass-conservation equation (1.4) and L substance equations of type (1.5) is straightforward. Equation (3.11) is almost unchanged, i.e.,

TABLE I

Limiting Coefficients for Various Cases

Case	β^A	β^ρ
Eq. (3.10a) with $a_{i,j}^{\min} \geq 0$	$\beta_{i,j}^{A,\mathrm{OUT}} \leq \dfrac{a_{i,j}^{\min}\rho_{i,j}^0 - A_{i,j}^0}{A_{i,j}^{\mathrm{out}} - a_{i,j}^{\min}\rho_{i,j}^{\mathrm{in}} - \varepsilon}$	$\beta_{i,j}^{\rho,\mathrm{IN}} \leq \beta_{i,j}^{A,\mathrm{OUT}}$
Eq. (3.10a) with $a_{i,j}^{\min} \leq 0$	$\beta_{i,j}^{A,\mathrm{OUT}} \leq \dfrac{a_{i,j}^{\min}\rho_{i,j}^0 - A_{i,j}^0}{A_{i,j}^{\mathrm{out}} - a_{i,j}^{\min}\rho_{i,j}^{\mathrm{out}} - \varepsilon}$	$\beta_{i,j}^{\rho,\mathrm{OUT}} \leq \beta_{i,j}^{A,\mathrm{OUT}}$
Eq. (3.10b) with $a_{i,j}^{\max} \geq 0$	$\beta_{i,j}^{A,\mathrm{IN}} \leq \dfrac{a_{i,j}^{\max}\rho_{i,j}^0 - A_{i,j}^0}{A_{i,j}^{\mathrm{in}} - a_{i,j}^{\max}\rho_{i,j}^{\mathrm{out}} + \varepsilon}$	$\beta_{i,j}^{\rho,\mathrm{OUT}} \leq \beta_{i,j}^{A,\mathrm{IN}}$
Eq. (3.10b) with $a_{i,j}^{\max} \leq 0$	$\beta_{i,j}^{A,\mathrm{IN}} \leq \dfrac{a_{i,j}^{\max}\rho_{i,j}^0 - A_{i,j}^0}{A_{i,j}^{\mathrm{in}} - a_{i,j}^{\max}\rho_{i,j}^{\mathrm{in}} + \varepsilon}$	$\beta_{i,j}^{\rho,\mathrm{IN}} \leq \beta_{i,j}^{A,\mathrm{IN}}$

$$\beta_{i,j}^{A_l,\mathrm{OUT}} = \frac{(a_l)_{i,j}^{\min}\rho_{i,j}^0 - (A_l^0)_{i,j}}{(A_l)_{i,j}^{\mathrm{out}} - [(a_l)_{i,j}^{\min}]^+\rho_{i,j}^{\mathrm{in}} - [(a_l)_{i,j}^{\min}]^-\rho_{i,j}^{\mathrm{out}} - \varepsilon} \tag{B10a}$$

$$\beta_{i,j}^{A_l,\mathrm{IN}} = \frac{(a_l)_{i,j}^{\max}\rho_{i,j}^0 - (A_l^0)_{i,j}}{(A_l)_{i,j}^{\mathrm{in}} - [(a_l)_{i,j}^{\max}]^+\rho_{i,j}^{\mathrm{in}} - [(a_l)_{i,j}^{\max}]^-\rho_{i,j}^{\mathrm{out}} + \varepsilon} \tag{B10b}$$

while there is a significant change to the correction coefficients (3.12) of the mass-conservation equation. They can be expressed with a conditional min statement of the form

$$\beta_{i,j}^{\rho,\mathrm{IN}} = \min_{1\leq l\leq L}\{\beta_{i,j}^{A_l,\mathrm{IN}} + \mathrm{sign}^+[(a_l)_{i,j}^{\max}], \beta_{i,j}^{A_l,\mathrm{OUT}} - \mathrm{sign}^-[(a_l)_{i,j}^{\min}]\} \tag{B11a}$$

$$\beta_{i,j}^{\rho,\mathrm{OUT}} = \min_{1\leq l\leq L}\{\beta_{i,j}^{A_l,\mathrm{OUT}} + \mathrm{sign}^+[(a_l)_{i,j}^{\min}], \beta_{i,j}^{A_l,\mathrm{IN}} - \mathrm{sign}^-[(a_l)_{i,j}^{\max}]\} \tag{B11b}$$

The complication arises since there are now $4L$ bounds of type (B6) for the coefficients β^ρ, which are the result of the four cases to be distinguished for each of the L substance equations.

APPENDIX C: USING THE MPDATA-ALGORITHM FOR THE TRANSPORT OF TWO-SIGNED QUANTITIES

The MPDATA algorithm [28] is a positive-definite conservative finite-difference scheme for the transport equation. In an attempt to use similar schemes for the transport of mass and momentum, the treatment in [28] was slightly generalized such as to be applicable to arbitrary fields (i.e., fields involving both positive and negative numbers). The changes involve the computation of the anti-diffusive velocities from

$$\tilde{u}_{i+(1/2)\mathbf{e}_l}^I \equiv [|u_{i+(1/2)\mathbf{e}_l}^I|\Delta X^I - \Delta t(u_{i+(1/2)\mathbf{e}_l}^I)^2] \times \frac{|\psi_{i+\mathbf{e}_l}^*| - |\psi_i^*|}{|\psi_{i+\mathbf{e}_l}^*| + |\psi_i^*| + \varepsilon} - \sum_{\substack{J=1\\J\neq 1}}^{M} 0.5\Delta t\, u_{i+(1/2)\mathbf{e}_l}^I \overline{u_{i+(1/2)\mathbf{e}_l}^I} \times \frac{|\psi_{i+\mathbf{e}_l+\mathbf{e}_J}^* + \psi_{i+\mathbf{e}_J}^*| - |\psi_{i+\mathbf{e}_l-\mathbf{e}_J}^* + \psi_{i-\mathbf{e}_J}^*|}{|\psi_{i+\mathbf{e}_l+\mathbf{e}_J}^* + \psi_{i+\mathbf{e}_J}^*| + |\psi_{i+\mathbf{e}_l-\mathbf{e}_J}^* + \psi_{i-\mathbf{e}_J}^*| + \varepsilon} \tag{C1}$$

instead of Eq. (13) in [28]. When using the generalized MPDATA algorithm with the nonoscillatory option, Eq. (15) in [31] must, in addition, be replaced with

$$\begin{aligned}\tilde{A}_{\mathbf{i}+(1/2)\mathbf{e}_l}^I &= [A_{\mathbf{i}+(1/2)\mathbf{e}_l}^I]^+ \times [\min(1, \beta_{\mathbf{i}}^{\downarrow}, \beta_{\mathbf{i}+\mathbf{e}_l}^{\uparrow})\mathrm{sign}(\psi_{\mathbf{i}})^+ \\ &\quad - \min(1, \beta_{\mathbf{i}}^{\uparrow}, \beta_{\mathbf{i}+\mathbf{e}_l}^{\downarrow})\mathrm{sign}(-\psi_{\mathbf{i}})^+] \\ &\quad + [A_{\mathbf{i}+(1/2)\mathbf{e}_l}^I]^- \times [\min(1, \beta_{\mathbf{i}}^{\uparrow}, \beta_{\mathbf{i}+\mathbf{e}_l}^{\downarrow})\mathrm{sign}(\psi_{\mathbf{i}+\mathbf{e}_l})^+ \\ &\quad - \min(1, \beta_{\mathbf{i}}^{\downarrow}, \beta_{\mathbf{i}+\mathbf{e}_l}^{\uparrow})\mathrm{sign}(-\psi_{\mathbf{i}+\mathbf{e}_l})^+].\end{aligned} \tag{C.2}$$

However, this form was not utilized in the synchronized flux correction described in Section 3, since in our case the flux correction is performed directly on the level of the fluxes rather than on the level of the anti-diffusive velocities as in [31].

The formulation given above is strictly sign-preserving when applied to purely positive or negative fields but, also, able to cope with fields involving both signs. Tests in one and two dimensions have revealed that the use of (C.1)–(C.2) gives virtually identical results as are obtained when splitting the field into positive and negative parts and transporting these fields individually with the standard formulation developed in [28, 31].

ACKNOWLEDGEMENTS

We thank Bernhard Müller, Dale R. Durran, and three anonymous reviewers for useful comments on earlier versions of the paper. This study has been originated while CS was the recipient of a postdoctoral fellowship from the Swiss National Science Foundation. Further support for CS has been provided by NSF under Grants ATM-8914138 and ATM-9106494.

REFERENCES

1. A. Arakawa and Y.-J. G. Hsu, *Mon. Weather Rev.* **118,** 1933 (1990).
2. R. Bleck, *Mon. Weather Rev.* **102,** 813 (1974).
3. R. Bleck, *Riv. Meteorol. Aeronaut.* **4,** 189 (1984).
4. R. Bleck and L. T. Smith, *J. Geophys. Res. C,* **95,** 3273 (1990).
5. D. L. Book, J. P. Boris, and K. Hain, *J. Comput. Phys.* **18,** 248 (1975).
6. J. P. Boris and D. L. Book, *J. Comput. Phys.* **11,** 38 (1973).

7. J. P. Boris and D. L. Book, *J. Comput. Phys.* **20,** 397 (1976).
8. H. C. Davies, *Mon. Weather Rev.* **111,** 1002 (1983).
9. C. Frei, *Tellus A* **45,** 44 (1993).
10. P. Gent, *J. Atmos. Sci.* **50,** 1323 (1993).
11. S. K. Godunov, *Math. Sb.* **47,** 271 (1959); Cornell Aero. Lab. Translation.
12. W. W. Grabowski and P. K. Smolarkiewicz, *Mon. Weather Rev.* **48,** 547 (1990).
13. V. Grubisic, R. B. Smith, and C. Schär, *J. Atmos. Sci.* **51,** (1994).
14. A. Harten and G. Zwaas, *J. Comput. Phys.* **9,** 568 (1972).
15. A. Harten, J. M. Hyman, and P. D. Lax, *Commun. Pure Appl. Math.* **29,** 297 (1976).
16. G. Hartjenstein and J. Egger, *Tellus A* **42,** 259 (1990).
17. J. B. Klemp and D. K. Lilly, *J. Atmos. Sci.* **35,** 78 (1978).
18. B. Larrouturou, *J. Comput. Phys.* **95,** 59 (1991).
19. R. Löhner, K. Morgan, J. Peraire, and M. Vahdati, *Int. J. Numer. Methods Fluids* **7,** 1093 (1987).
20. R. J. LeVeque, *SIAM J. Numer. Anal.* **33,** 627 (1996).
21. P. P. Miller and D. R. Durran, *J. Atmos. Sci.* **48,** 1457 (1991).
22. M. L. Merriam, Ames Research Center, Report No. NASA TM-101086, 1989 (unpublished).
23. J. M. Reisner and P. K. Smolarkiewicz, *J. Atmos. Sci.* **51,** 117 (1994).
24. P. J. Roache, *Computational Fluid Dynamics* (Hermosa, Albuquerque, NM, (1972).
25. C. Schär and R. B. Smith, *J. Atmos. Sci.* **50,** 1373 (1993).
26. C. Schär and R. B. Smith, *J. Atmos. Sci.* **50,** 1401 (1993).
27. R. B. Smith, *J. Atmos. Sci.* **45,** 3889 (1989).
28. P. K. Smolarkiewicz, *J. Comput. Phys.* **54,** 325 (1984).
29. P. K. Smolarkiewicz, *Mon. Weather Rev.* **119,** 2505 (1991).
30. P. K. Smolarkiewicz, "Nonoscillatory Advection Schemes," in *Proceedings, Seminar on Numerical Methods in Atmospheric Models*, Vol. I (ECMWF, Reading, UK, 1991), p. 235.
31. P. K. Smolarkiewicz and W. W. Grabowski, *J. Comput. Phys.* **86,** 355 (1990).
32. P. K. Smolarkiewicz and G. A. Grell, *J. Comput. Phys.* **101,** 431 (1992).
33. P. K. Smolarkiewicz and L. G. Margolin, *Mon. Weather Rev.* **121,** 1847 (1993).
34. P. K. Smolarkiewicz and J. A. Pudykiewicz, *J. Atmos. Sci.* **49,** 2082 (1992).
35. S. T. Zalesak, "A Preliminary Comparison of Modern Shock-Capturing Schemes: Linear Advection," in *Advances in Computer Methods for Partial Differential Equations*, Vol. VI, edited by R. Vichnevetsky and R. Stepleman, Publ. IMACS (Baltzer, Basel, 1987).
36. S. T. Zalesak, *J. Comput. Phys.* **31,** 335 (1979).